



## Quasi-steady circulation regimes in the Baltic Sea

1

2 **Taavi Liblik<sup>1</sup>, Germo Väli<sup>1</sup>, Kai Salm<sup>1</sup>, Jaan Laanemets<sup>1</sup>, Madis-Jaak Lilover<sup>1</sup>, Urmas Lips<sup>1</sup>**

3

4 <sup>1</sup>Department of Marine Systems, Tallinn University of Technology, Tallinn, Estonia

5 **\* Correspondence:**

6 Taavi Liblik

7 taavi.liblik@taltech.ee

8 **Keywords: Circulation, ADCP, underwater glider, Baltic Sea, boundary current, geostrophic**  
9 **current, upwelling-downwelling.**

10 **Abstract.** Circulation plays an essential role in the creation of physical and biogeochemical fluxes in  
11 the Baltic Sea. The main aim of the work was to study the quasi-steady circulation patterns under  
12 prevailing forcing conditions.

13 Six months of continuous vertical profiling and fixed-point measurements of currents, two monthly  
14 underwater glider surveys, and numerical modelling were applied in the central Baltic Sea. The vertical  
15 structure of currents was strongly linked to the location of the two pycnoclines: the seasonal  
16 thermocline and the halocline. The vertical movements of pycnoclines and velocity shear maxima were  
17 synchronous. The quasi-steady circulation patterns were in geostrophic balance and high-persistent.  
18 The persistent patterns included circulation features such as upwelling, downwelling, boundary  
19 current, and sub-halocline gravity current. The patterns had a prevailing zonal scale of 5–60 km and  
20 considerably higher magnitude and different direction than the long-term mean circulation pattern.

21 Northward (southward) geostrophic boundary current in the upper layer was observed along the eastern  
22 coast of the central Baltic in the case of southwesterly (northerly) wind. The geostrophic current at the  
23 boundary was often a consequence of wind-driven, across-shore advection.

24 The sub-halocline quasi-permanent gravity current with a width of 10–30 km from the Gotland Deep  
25 to the north over the narrow sill separating the Farö Deep and Northern Deep was detected in the  
26 simulation, and it was confirmed by an Argo float trajectory. According to the simulation, a strong  
27 flow, mostly to the north, with a zonal scale of 5 km occurred at the sill. This current is an important  
28 deeper limb of the overturning circulation of the Baltic Sea. The current is stronger with northerly  
29 winds and restricted by the southwesterly winds.

30 The circulation regime has an annual cycle due to seasonality in the forcing. Boundary currents are  
31 stronger and more frequently northward during the winter period. The sub-halocline current towards  
32 the north is strongest in March–May and weakest in November–December.

33

34



## 35 1 Introduction

36

37 Current structure is an important player in the physical and biogeochemical fluxes in ocean. The semi-  
38 enclosed, shallow, brackish Baltic Sea has a strong but variable vertical stratification characterized by  
39 two pycnoclines: the permanent halocline and the seasonal thermocline (Leppäranta & Myrberg, 2009).  
40 Three-layer structure occurs in summer and consists of warm and fresh upper mixed layer, cold and  
41 saltier intermediate layer, and warmer and saltiest deep layer. Water column is mixed up to the  
42 permanent halocline at 60–80 m depth and cold intermediate water forms during winters. Stratification  
43 through the two pycnoclines impedes vertical mixing, and transport of substances between the layers  
44 is limited. The role of tides is marginal in the Baltic Sea. Lateral flows play an important role in  
45 distributing the water properties.

46 Water-mass circulation of the Baltic Sea is determined by the saline water inflow from the North Sea  
47 and freshwater input from the catchment area. The interaction of the fresher and saltier waters forms  
48 the so-called Baltic haline conveyor belt (Döös et al., 2004). The belt consists of saltier water transport  
49 and signal propagation in the deep layer towards the north-eastern end of the Baltic (Liblik et al., 2018;  
50 Väli et al., 2013); upward salt flux through vertical mixing and transport (Reissmann et al., 2009), and  
51 outflow of the mix of riverine and saltier water in the upper layer (Jakobsen et al., 2010). The conveyor  
52 determines salinity, stratification and other important characteristics for the pelagic ecosystem.

53 The largest basin in the sea, the Baltic Proper (Fig. 1a) is a source for the deep waters of the Gulf of  
54 Riga, Gulf of Finland and Gulf of Bothnia. Permanent oxygen depletion has expanded in recent decades  
55 in the Baltic Sea, forming one of the largest dead zones in the global ocean (e.g. Carstensen et al.,  
56 2014). Only Major Baltic Inflows (Matthäus & Franck, 1992; Mohrholz, 2018) ventilate the deep layers  
57 of the southern and central Baltic Proper (Holtermann et al., 2017) but increase hypoxia in the Northern  
58 Baltic Proper and Gulf of Finland (Liblik et al., 2018).

59 The basin-scale pattern of the long-term mean circulation in the Baltic Proper is cyclonic as  
60 demonstrated by several modelling studies (Hinrichsen et al., 2018; Jedrasik et al., 2008; Jędrasik &  
61 Kowalewski, 2019; Meier, 2007; Placke et al., 2018). The mean circulation is to the north along the  
62 eastern coast of the Baltic Proper and to the south along the eastern and western coast of Gotland Island  
63 (Meier, 2007; Placke et al., 2018). The turning area for this basin-wide cyclonic circulation cell in the  
64 north is between 59 to 59.5° N (Meier, 2007). The zonal center of the cyclonic flow in the Eastern  
65 Gotland Basin is in the Gotland Deep (Placke et al., 2018). The cyclonic structure exists from the  
66 bottom to the surface (Placke et al., 2018), although lateral structure and magnitude of the flow vary  
67 among different models (Placke et al., 2018). It is important to note that all forementioned descriptors  
68 of the long-term mean flow rely on numerical simulations and lack support from observations.  
69 However, a consistent northward low-frequency current along the eastern slope of the Gotland Deep  
70 at 204 m depth has been reported (Hagen & Feistel, 2004). Placke et al. (2018) compared simulated  
71 currents with these measurements. All model simulations showed the mean meridional northward  
72 current velocity in the range of 0–1 cm s<sup>-1</sup> (actually, three models out of four had values of 0.0–0.1 cm  
73 s<sup>-1</sup>) while the measurements gave the mean northward velocity of 3 cm s<sup>-1</sup> (Hagen & Feistel, 2004).  
74 Thus, the long-term mean flow to north in the deep layer was much stronger than the simulated mean  
75 current.

76 Temporal variability of currents in the Baltic Sea is very high as a reaction to atmospheric forcing.  
77 Near-shore Eulerian current observations (Sokolov & Chubarenko, 2012) and drifter experiments

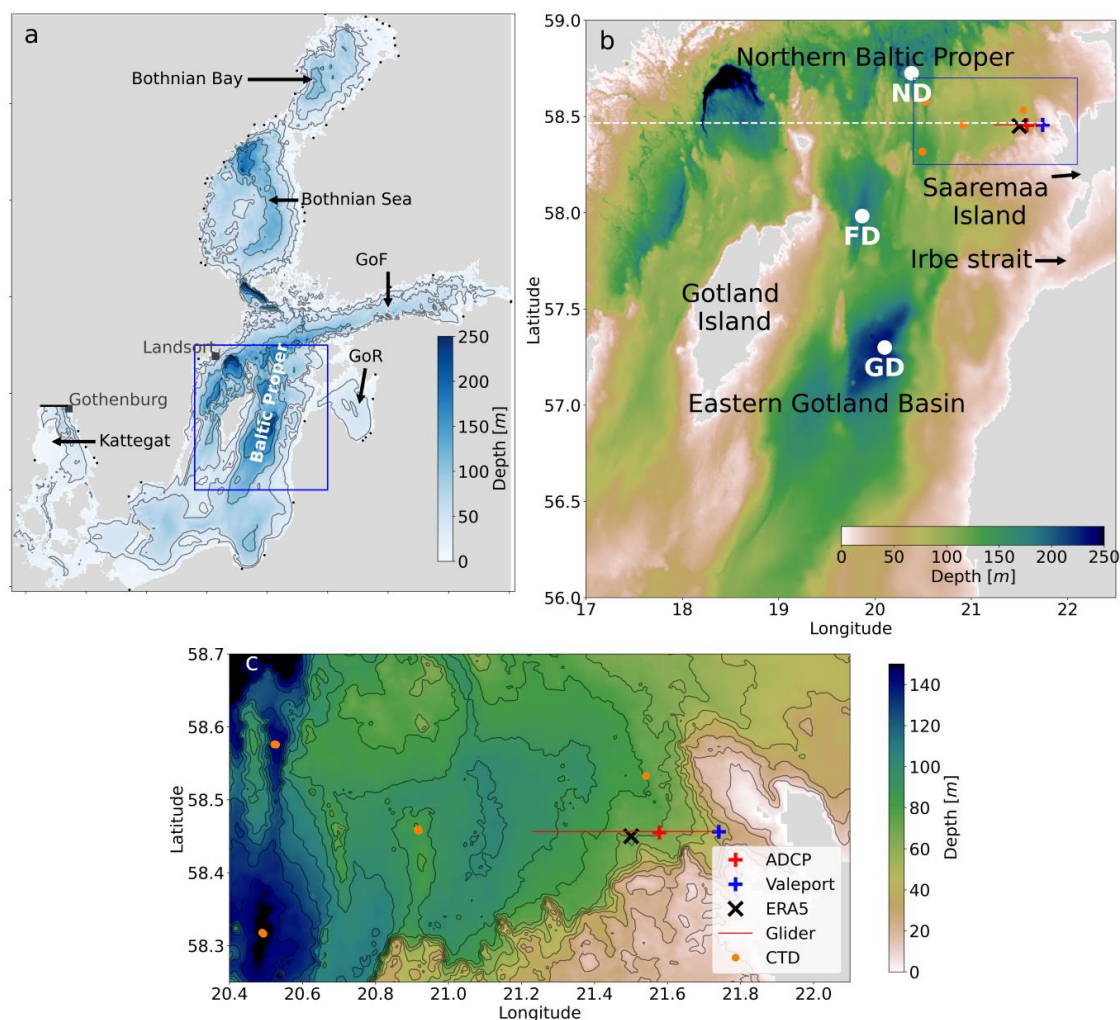


78 (Golenko et al., 2017; Krayushkin et al., 2019) conducted in the southern Baltic Proper showed a strong  
79 correlation between wind and surface currents. Current velocity spectra in the Baltic include seiches  
80 and tides with different periods from 11 h to 31 h and inertial motions with a period of about 14 h  
81 (Jönsson et al., 2008; Lilover et al., 2011; Suhhova et al., 2018).

82 The vertical current structure through thermocline and halocline has not been rigorously studied by the  
83 in-situ observations in the Baltic Proper. Moreover, despite a considerable effort to reveal the spatial,  
84 long-term mean circulation patterns based on the simulations, not much has been done to study  
85 temporal developments of currents in the synoptic (mesoscale) and seasonal timescales in the Baltic  
86 Proper. In the present work, we address this shortage of knowledge.

87 Permanent circulation systems, such as boundary currents or subtropical gyres, are key processes that  
88 determine transport in the open ocean (e.g. Macdonald, 1998). Although there are no permanent  
89 currents in the Baltic Sea, we hypothesize that under stable wind forcing and stratification conditions,  
90 a steady circulation regime prevails in the time-scale of days to weeks and has a much greater  
91 magnitude than the mean current structures. These quasi-steady circulation features could be related to  
92 the downwelling and upwelling processes or appear as a boundary current or a gravity current under  
93 the halocline.

94 Following a description of the methods used, we present an analysis of (1) boundary current under  
95 variable wind forcing and stratification, (2) quasi-permanent circulation patterns, and (3) sub-halocline  
96 current. The analysis of observational and simulation results is followed by discussion and conclusions.



97

98 **Figure 1.** (a) Map of the Baltic sea and model domain. Shown are the locations of the open boundary of the  
99 model domain in the Kattegat (bold black line), Landsort and Gothenburg sea level stations, Baltic Sea rivers  
100 used in the model (black dots) and study area (black box). (b) Close-up of the study area. Locations of ADCP  
101 and Valeport moorings, CTD measurements, glider section, the center of the cell of ERA5 wind data, and zonal  
102 section along the latitude of the ADCP location in the Northern Baltic Proper (white dashed line) are presented.  
103 Gotland Deep (GD), Fårö Deep (FD) and Northern Deep (ND) are also shown. (c) Close view of the moorings  
104 and CTD measurement locations, glider section, and local topography are shown.

105

## 106 2 Data and methods

### 107 2.1 Observations and data products

108 A bottom mounted current profiler ADCP 300 kHz (Teledyne RDI) and model 106 current meter  
109 (Valeport Ltd) (hereinafter referred to as Valeport) were deployed at the end of February to the west of  
110 Saaremaa Island (Fig. 1b and c). Valeport was mounted at 5 m depth, while the sea bottom depth in its



111 location was 41 m. The sea depth in the ADCP location was 71 m and velocities were measured with  
112 vertical depth interval of 2 m in the depth range of 10–68 m. Current velocity profiles were recorded  
113 as average of 1 h. The quality of the current velocity data was checked following the procedure  
114 developed by Book (et al., 2007). Valeport recorded current velocity with 10 min intervals. A Seabird  
115 SBE 16*Plus* V2 CTD SEACAT conductivity and temperature recorder was deployed together with the  
116 ADCP, but it hung 4 m above the sea bottom, i.e., at a depth of 67 m. SBE 16*Plus* sensors were  
117 calibrated by the manufacturer before the deployment.

118 Repeated CTD profiles onboard R/V *Salme* were collected using an OS320 CTD probe (Idronaut S.r.l.)  
119 in the Northern Baltic Proper (see Fig. 1b and c) from 30 January to 4 August 2020.

120 Argo float deployment was arranged by the Finnish Meteorological Institute (Siiriä et al., 2019) from  
121 15 August 2013 to 15 August 2014 and the trajectory data was derived from the Argo-based deep  
122 displacement dataset (Ollitrault & Rannou, 2013). The dataset was downloaded on 15 March 2021 at  
123 <https://www.seanoe.org/data/00360/47077/>.

124 In 2020, two glider missions were conducted in the Northern Baltic Proper. The Slocum G2 Glider  
125 collected oceanographic data along the E–W oriented 27 km long section (Fig. 1b and c). The  
126 easternmost point of the glider track was approximately 7 km off the shoreline and the section was  
127 located at the sloping bottom where sea depth gradually deepened westward from 40 m to 90 m. The  
128 first mission was carried out from 28 February to 22 March 2020 and the second one from 4 August to  
129 2 September 2020. Both ascending and descending profiles were recorded and altogether over 8000  
130 profiles were gathered. The glider moved at a horizontal speed of  $0.33 \pm 0.08 \text{ m s}^{-1}$ . On average, a profile  
131 took  $8.0 \pm 0.9$  min to complete 80–90 m deep profile and the average distance between the profiles near  
132 the surface was  $301 \pm 46$  m. Both the sampling time and the distance were decreased by half in the  
133 shallow part of the section.

134 Preliminary glider data processing included the standard quality control (impossible date and location  
135 test, range tests for the sensors) and accounting for the response time of the sensors and the thermal  
136 lag. First, a linear time shift was applied to temperature and conductivity considering the misalignment  
137 with pressure. Temperature was re-aligned by 1.4 s and conductivity by 0.9 s for the mission conducted  
138 in the spring and respectively by 1.6 s and 1.1 s for the mission in the summer. The parameters were  
139 chosen by comparing consecutive profiles focusing on the depth range around the greatest gradient. It  
140 was assumed that successive profiles correspond to the same water mass. We followed Mensah et al.  
141 (2009) to remove the thermal lag effect and found optimal coefficients for the temperature error  
142 amplitude,  $\alpha$ , and time constant,  $t_c$ , by comparing consecutive TS-profiles. The satisfying results were  
143 obtained in the case of  $\alpha = 0.0025$  and  $t_c = 10$  s for the earlier mission and  $\alpha = 0.055$  and  $t_c = 12$  s for  
144 the following one. The profiles were averaged on a 0.5 dbar vertical grid after processing the raw data.

145

146 Sea surface temperature was derived from the Copernicus Marine Service product  
147 SST\_BAL\_SST\_L4\_REP\_OBSERVATIONS\_010\_016 with a horizontal resolution of  $0.02 \times 0.02$   
148 degrees. Mean difference between the product and in-situ data sources has been in the range of  $-0.12$   
149 to  $-0.21$  °C and root mean square error from 0.43 to 0.88 °C depending on the data sources according  
150 to the quality information document  
151 (<https://catalogue.marine.copernicus.eu/documents/QUID/CMEMS-SST-QUID-010-016.pdf>,  
152 accessed 19 August 2021).



153 Hourly, 10 m level wind velocities of ERA5 reanalysis data (Hersbach et al., 2020) at the cell with the  
154 size  $0.25^{\circ} \times 0.25^{\circ}$  from 1979 to 2020 (see Fig. 1 for location) were used in the analyses.

155

## 156 **2.2 Modelling**

157 Numerical model GETM (General Estuarine Transport Model, Burchard & Bolding, 2002) has been  
158 applied to simulate the circulation and temperature/salinity distribution in the northeastern Baltic Sea.  
159 GETM is a primitive equation, three-dimensional model with free surface and  $k-\varepsilon$  turbulence model  
160 for vertical mixing by coupling the hydrodynamic part with GOTM (General Ocean Turbulence Model,  
161 Umlauf & Burchard, 2005).

162 Model domain covered the whole Baltic Sea with the open boundary situated in the Kattegat region  
163 (Fig. 1a). The horizontal grid spacing of the model was 0.5 nautical miles (926 m) and 60 vertically  
164 adaptive coordinates (Hofmeister et al., 2010; Gräwe et al. 2015) were used. Sea surface height from  
165 Gothenburg station has been used as the boundary condition to control the barotropic in- and outflow  
166 from the Baltic Sea, while the temperature and salinity were nudged towards monthly climatological  
167 profiles (Janssen et al., 1999) along the open boundary.

168 Data from the Estonian version of the operational model HIRLAM (High Resolution Limited Area  
169 Model) maintained by the Estonian Weather Service and giving forecasts with hourly resolution  
170 (Männik and Merilain, 2007) were used to calculate the momentum and heat flux at the sea surface.  
171 Climatological runoff of the Baltic Sea rivers with inter-annual variability added from the values  
172 reported to the HELCOM (Johansson, 2016) was used. Simulation covered period from April 2010 to  
173 September 2020, and initial temperature and salinity fields were taken from the CMEMS (Copernicus  
174 Marine Service) re-analysis product for the Baltic Sea.

175 The same setup of the model was previously used in Zhurbas et al., (2018) and Liblik et al. (2020) and  
176 more details about the model setup are given there. Zhurbas et al. (2018) validated the salinity and  
177 temperature values in the central Baltic Sea along with the sea surface height at Landsort station and  
178 compared the near-bottom current statistics with the long-term observations in the Gotland Deep.  
179 Liblik et al. (2020) validated the simulated wintertime sea surface temperature and salinity in the Gulf  
180 of Finland and compared the observed mixed layer depth with the simulations. In this study, we will  
181 present the comparison of simulated and observed currents in the Northern Baltic Proper.

182

## 183 **2.3 Calculations**

184 Isohaline  $9 \text{ g kg}^{-1}$  was selected to define the center of the halocline (CH) depth since the halocline was  
185 steepest around this salinity value according to the salinity profiles. To estimate the center of halocline  
186 depth based on single level salinity time-series measured by the SBE 16*Plus*, and twelve CTD profiles  
187 collected by the RV Salme in the Northern Baltic Proper (see Fig. 1b) from 30 January to 4 August  
188 2020 were used. Salinity profiles were vertically normalized by subtracting the depth of the CH at each  
189 profile. Next, the mean salinity profile in the normalized depth coordinates was calculated (Fig. 2). The  
190 mean normalized depth and salinity relationship were used to derive the CH depth from the SBE 16*Plus*  
191 salinity time-series at 67 m depth. If salinity was lower (higher) than  $9 \text{ g kg}^{-1}$ , the CH was deeper  
192 (shallower) than 67 m according to the mean depth-salinity curve (Fig. 2). Maximum depth of the  
193 neighboring sea area, 88 m, was defined as the maximum depth of the CH.



194 In this study the  $x$ -axis is positive eastward, the  $y$ -axis is positive northward, and the  $z$ -axis is positive  
195 upward ( $z=0$  at the sea surface),  $u$  and  $v$  are horizontal velocity components.

196 The baroclinic components of the geostrophic velocity ( $u_g$  and  $v_g$ ) can be deduced from the  
197 hydrographic data. Considering the dynamic method, the geostrophic relationships are as follows

198 
$$v_g = \frac{1}{f} \frac{\partial \Phi}{\partial x}$$

199 
$$u_g = -\frac{1}{f} \frac{\partial \Phi}{\partial y}$$

200 The geopotential,  $\Phi$ , is proportional to the dynamic height,  $D$ , as

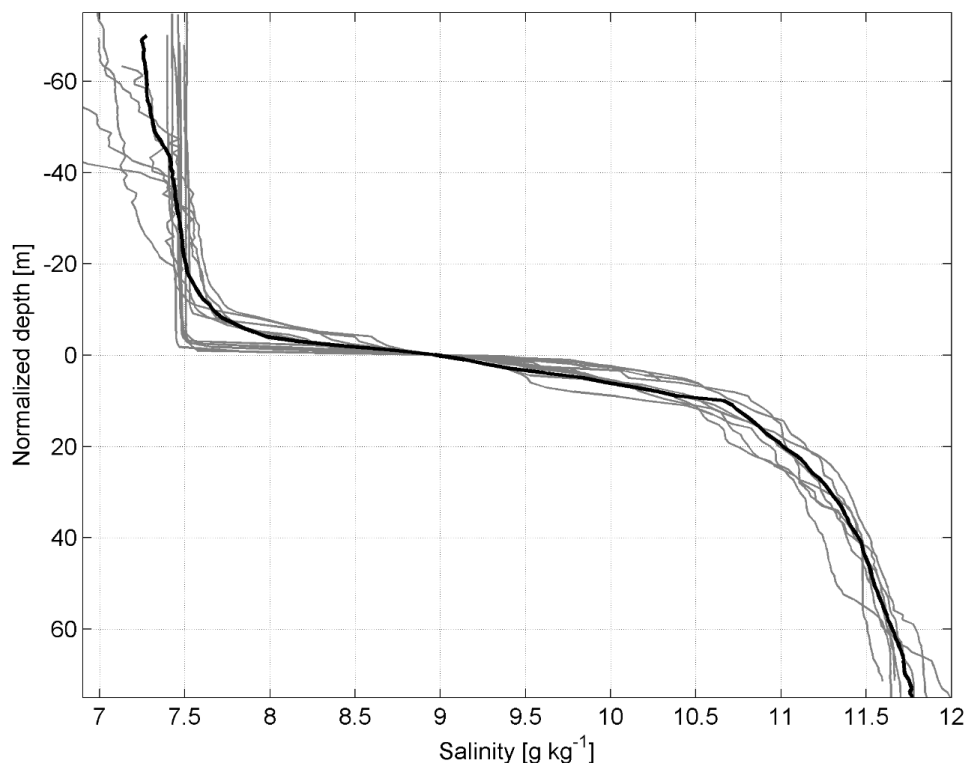
201 
$$\Phi = gD$$

202 where  $g$  is the gravitational acceleration and  $f$  is the Coriolis parameter.

203 The dynamic height can be determined from the temperature and salinity (density) profiles.

204 The relative geostrophic velocity was evaluated using dynamic height anomaly relative to a reference  
205 pressure (McDougall & Barker, 2011). The geopotential slope of an isobaric surface expresses the  
206 horizontal pressure gradient. A zonal glider track enabled to calculate the meridional velocity profile  
207 of the geostrophic flow. The meridional geostrophic velocity was calculated also from the GETM  
208 simulation data. The reference level was set at 70 dbar. The shallower profiles were included using the  
209 stepped no-motion level method described in Rubio et al. (2009). Since velocity is not zero at the 70  
210 dbar level, the calculated geostrophic velocities  $V_{\text{GEO-DENS-glider}}$  and  $V_{\text{GEO-DENS-GETM}}$  described in  
211 subchapter 3.1 represent relative velocities to the no-motion 70 dbar level. Both variables represent an  
212 averaged velocity at an extent of 10 km zonal scale around ADCP position.

213 To compare the simulated geostrophic velocity profiles with the measured ADCP velocity profiles, the  
214 relative geostrophic velocity at the sea surface (calculated relative to 70 dbar using simulated density  
215 profiles) was aligned with the geostrophic velocity due to the sea level gradient from the model  
216 simulation ( $V_{\text{GEO-SL-GETM}}$ ). Sea level gradient was estimated from linear regression fit of sea level  
217 anomalies at a horizontal scale of 10 km. The difference (vector) between the density-estimated and  
218 the sea level estimated geostrophic velocity at the sea surface was applied to the whole geostrophic  
219 velocity profile under the assumption that the geostrophic current at the surface is determined by the  
220 differences in the sea level exclusively. Adjusted geostrophic velocity profiles were presented as  $V_{\text{GEO-}}$   
221  $\text{ADI-GETM}$  in subchapter 3.2.



222

223 **Figure 2.** Vertically normalized salinity profiles from 30 January to 4 August 2020 in the Northern Baltic Proper  
224 (see Fig. 1b). Bold black line represents the mean salinity profile.

225 The direct influence of wind forcing on the subsurface currents was ascertained using the classical  
226 Ekman model based on the balance of the frictional and Coriolis forces (Ekman, 1905). Wind stress  
227 vector  $\tau$  as the Ekman model input parameter was calculated using ERA5 (Fig. 1b and c) wind data:  $\tau$   
228 =  $\rho_{\text{air}}cd|\mathbf{U}|\mathbf{U}$ , which were prior low-pass filtered with cut-off 36 hours to exclude periodic processes.  
229 Here  $\mathbf{U}$  is the wind velocity vector at 10 m height,  $cd$  is the drag coefficient and was parameterized as  
230 proposed by (Wu, 1980):  $cd=(0.8+0.065|\mathbf{U}|)\times 10^{-3}$ ,  $|\mathbf{U}|$  is the wind velocity vector module and  $\rho_{\text{air}}$  is the  
231 density of air. The eddy viscosity used in the model was calculated according to (Csanady,  
232 1981):  $\nu = |\tau|/200f$ , where  $|\tau|$  is the wind stress vector module. The model outputs are the vertical  
233 profiles of wind-induced current velocity components.

234 The temporal development in the vertical current structure is presented as the time-series of vertical  
235 current shear squared  $s^2 = (\partial u/\partial z)^2 + (\partial v/\partial z)^2$ .

236 Persistency of the current is defined as the ratio between vector and scalar current speeds:

237 
$$R = \frac{\sqrt{u^2+v^2}}{\frac{1}{N}\sum\sqrt{u_n^2+v_n^2}}$$

238





239 Current and wind velocity components are presented as 36-h and 10-day low-passed time-series. The  
240 fourth-order Butterworth filter was used for low-pass filtering.

## 241 3 Results

### 242 3.1 Boundary current under variable wind forcing

243 Statistics of the 6 months (1 March–1 September 2020) ADCP deployment revealed the persistency of  
244 currents between 32 and 42%, with the highest persistency in the 20–40 m depth range (Table 1). Mean  
245 and maximum hourly measured speeds were higher in the uppermost bin at 11 m depth, 11 and 48 cm  
246  $s^{-1}$ , respectively and lower in the near-bottom layer, 7 and 34  $cm s^{-1}$ . The mean  $u$ - and  $v$ -components  
247 were positive in all depths showing the mean flow to the NE sector.

248 From the flow structure point of view the ADCP current velocity time series can be divided into two  
249 periods: 1) from March until mid-April, when barotropic regime prevailed, 2) from mid-April until  
250 September, when layered flow dominated (Fig. 3a and b). One can also see the coincidence of the  
251 current  $u$ - and  $v$ -components in the uppermost and deepest bin during the first period (Fig. 3c and d)  
252 except a short period at the end of March. Discrepancies between the two layers afterwards illustrated  
253 the layered, baroclinic nature of the flow. The flow regime reacted well to wind forcing. Barotropic  
254 flow to the northeast prevailed as a result of southwesterly winds until mid-April (Fig. 4). Only during  
255 the last week of March, when wind was from northerly directions, a strong southerly current was  
256 observed. Similar temporal patterns appeared in the upper layer in the stratified period. Alteration of  
257 positive and negative meridional velocities was related to the prevailing wind direction. These  
258 tendencies were evident both in the ADCP and Valeport locations. Deep layer current was directed to  
259 the east, i.e., onshore, when southerly flow occurred in the upper layer and to the west or southwest,  
260 when the current to the northeast prevailed. These are signs of the layered structure of the coastal  
261 upwelling and downwelling.

262 The most frequent current direction in the upper layer (11 m depth) was  $40^\circ$  at the ADCP location. To  
263 estimate the relationship between the low-frequency (10-day low-passed) current component and wind,  
264 we calculated the correlation between the  $40^\circ$  current velocity component ( $c_{40}$ ) in the upper layer and  
265 wind speed from different directions with different time lags. The best correlation ( $r^2=0.65$ ,  $p<10^{-100}$ ,  
266  $n=4473$ ) was found with the wind from the south, specifically towards  $10^\circ$  ( $w_{10}$ ), applying a 3-day time  
267 lag. This, on the one hand, corresponds to Ekman's theory, however, on the other hand, the 3-day delay  
268 is rather long. Probably it can be explained by the mixed effect of wind on the surface currents. The  
269 momentum flux created by wind impacts the current field fast. The correlation without delay is  
270 relatively high ( $r^2=0.55$ ,  $p<10^{-100}$ ,  $n=4473$ ) as well. The flow resulting from the sea level gradient and  
271 due to the inclination of isopycnal surfaces are also a consequence of wind but develop slower.

272 Time series of  $c_{40}$  reveal negative values from mid-April until the end of June (Fig. 3e). Before mid-  
273 March and in July–August, the  $c_{40}$  was mostly positive. The main course of  $w_{10}$  and  $c_{40}$  coincided well,  
274 but discrepancies occurred in the details. For instance, negative  $c_{40}$  occurred when  $w_{10}$  was positive in  
275 the ADCP location in the last third of March and first half of May. The mean values of  $w_{10}$  and  $c_{40}$   
276 during the measurements were  $0.6 m s^{-1}$  and  $3.2 cm s^{-1}$ , respectively. Considering the linear relation  
277 between the two variables, the 1979–2020 mean  $w_{10} = 1.1 m s^{-1}$  corresponds to  $c_{40} = 4.2 cm s^{-1}$ .

278 The most frequent current direction was  $350^\circ$  at the Valeport location. The discrepancy between the  
279 dominant flow direction at the ADCP and Valeport locations is related to the topographic features (Fig.  
280 1). However, from the wider Baltic Sea dynamics point of view the meridional current component is  
281 important to investigate. To study the temporal developments of the meridional current, we next



282 analyze the measured and simulated meridional current components at 11 m depth at the ADCP  
283 location,  $V_{\text{ADCP}}$  and  $V_{\text{GETM}}$ . We also calculated the geostrophic component  $V_{\text{GEO-SL-GETM}}$  of the current  
284 velocity from the simulated sea level gradient, relative geostrophic meridional current component  
285 ( $V_{\text{GEO-DENS-GETM}}$ ) at 11 m depth based on simulated temperature and salinity data in the section and  
286 same for the glider temperature and salinity data ( $V_{\text{GEO-DENS-glider}}$ ). We also calculated mean Ekman  
287 current  $u$ - and  $v$ -components in the depth range 0–10 m  $U_{\text{Ekman}}$  and  $V_{\text{Ekman}}$ , respectively. All parameters  
288 are 36-h low-passed filtered.

289 Overall, the simulated  $V_{\text{GETM}}$  reasonably well follows the temporal changes in measured  $V_{\text{ADCP}}$  (Fig.  
290 5).  $V_{\text{GETM}}$  tends to have smaller values than  $V_{\text{ADCP}}$ , which means that the meridional component of  
291 simulated velocity is biased southward. Sometimes, e.g., in June and August, the discrepancies are  
292 considerable. Geostrophic current  $V_{\text{GEO-DENS-GETM}}$  was very small, and  $V_{\text{GEO-DENS-glider}}$  was practically  
293 zero in March (Fig. 5b) as the water column was mixed down to the reference depth of the geostrophic  
294 current calculation. Since the end of March, overall temporal developments in the meridional current  
295 ( $V_{\text{ADCP}}$  and  $V_{\text{GETM}}$ ) and its geostrophic components ( $V_{\text{GEO-DENS-GETM}}$ ), ( $V_{\text{GEO-SL-GETM}}$ ) and  $V_{\text{GEO-DENS-}}$   
296  $glider$ ) in August match quite well (Fig. 5a and b). This can be related to the multiple effects of wind.  
297 South-westerly wind resulted in the Ekman current towards the eastern coast of the Northern Baltic  
298 Proper. This caused, first, a sea level gradient across the basin (higher near the coast), which induced  
299 barotropic current to the north. Secondly, it evoked downwelling along the coast and resulted in a  
300 vertical gradient of the geostrophic current. Such events were detected at the beginning of April and  
301 July, when strong southwesterly winds blew (Fig. 4) and caused Ekman current towards the coast (Fig.  
302 5c). Northerly or northeasterly winds caused opposite effects. Sea level was lower near the coast  
303 compared to offshore and thermocline was located at shallower depths near the coast. Thus, the flow  
304 was directed to the south in the surface layer. Such events occurred in late March and mid-August.  
305 Most of the major events of the positive  $V_{\text{ADCP}}$  and  $V_{\text{GETM}}$  were associated with the positive  $u$ -  
306 component of the Ekman current (cf. Fig. 5a and c), i.e., flow towards the shore, not along the shore.  
307 Thus, the wind-driven strong coastal current to the north is not induced by the direct momentum flux  
308 created by wind stress but rather is the result of wind-driven sea level gradient and depression of the  
309 pycnoclines at the coast, which resulted in vertically sheared geostrophic current.

310 Next, we consider the relationship between the vertical maxima of the current shear and the vertical  
311 location of pycnoclines – seasonal thermocline and halocline. Seasonal thermocline began to develop  
312 from the beginning of May (Fig. 6a). The temporal course of salinity at 67 m depth (Fig. 6b) and depth  
313 of halocline center (CH) (Fig. 6d) showed that halocline was mostly located deeper than the deepest  
314 ADCP bin. At the end of March, the halocline center reached 55 m depth (Fig. 6d) and high current  
315 shear values were observed below 45 m depth (Fig. 6c). Shallower halocline was related to the  
316 northerly wind event (Fig. 4), which caused offshore Ekman transport in the upper layer and  
317 compensating onshore flow in the deep layer (Fig. 3). Such events of high current shear in the deep  
318 layer also occurred at the end of April to early May, from the end of May to mid-June and in mid-  
319 August (Fig. 6c) when the halocline center was shallower, and salinity increased at 67 m depth. Note  
320 that the depth of the halocline center and shear maxima were vertically shifted, halocline center was  
321 deeper. This can be explained by the vertical range of the halocline. The upper boundary of the  
322 halocline is shallower than the center of the halocline. Thus, the shear maxima were rather linked to  
323 the upper boundary of the halocline.

324 Stronger and more extensive shear maxima in the upper part of the water column were observed since  
325 late April (Fig. 6c). It appeared days before thermal stratification developed. One could see that SST  
326 (sea surface temperature) and temperature at 67 m depth coincided until the end of April. The  
327 occurrence of earlier shear maxima could be explained by the formation of the stratification in the



328 upper layer caused by the transport of fresher surface water to the area due to northerly wind forcing.  
329 Shear maxima became stronger in the second half of May when thermal stratification developed.  
330 Strong downwelling and likely also vertical mixing occurred in July as a result of a strong  
331 southwesterly wind impulse with the duration of more than a week (Fig. 4). This can be seen as a drop  
332 in SST from 21 to 15 °C and occasional high temperature recordings in the deep layer (Fig. 6a). The  
333 latter indicates that the upper layer water arrived at the 67 m deep measurement spot. This event is well  
334 reflected in the time series of current shear. Deepening of the shear maxima down to 50–55 m depth  
335 (Fig. 6c) occurred together with thermocline deepening, as the near-bottom temperature recordings  
336 suggest. Relaxation of the downwelling occurred in mid-July, and another downwelling developed at  
337 the end of July. The linkage between the thermocline and shear maxima was well seen in August when  
338 glider observations were available. The thermocline and shear maxima reached down to 40 m depth in  
339 the beginning and the end of the month, while they were located at 20 m depth in the middle of the  
340 month (Fig. 6a and c). The vertical movements of the halocline (Fig. 6d) and thermocline and linked  
341 shear maxima were synchronized. As thermocline, the halocline had its position also shallower in mid-  
342 August and deeper before and after. Note that downwelling was initiated by strong southerly,  
343 southwesterly or westerly winds and all events were seen as a SST decrease, likely due to vertical  
344 mixing, decrease in salinity at 67 m depth and deepening of the thermocline and halocline and related  
345 shear maxima. Relaxation of downwelling occurred when northerly winds or calmer periods prevailed  
346 and appeared as an increase in SST and upward movement of both pycnoclines.

347 Thus, we can conclude that the vertical structure of currents was strongly linked to the varying depths  
348 of pycnoclines, which were sensitive to wind forcing.

349 **Table 1.** Statistics of the 1-h average ADCP current data from 28 February to 2 September 2020.

Depth (m)	Mean speed (cm s <sup>-1</sup> )	Mean <i>u</i> (cm s <sup>-1</sup> )	Mean <i>v</i> (cm s <sup>-1</sup> )	Maximum speed (cm s <sup>-1</sup> )	Persistency (%)
10.8	11.3	3.8	1.1	48	35.1
20.8	10.2	4	1.7	44	42.3
30.8	9.5	3.7	1.4	38	41.7
40.8	9	3.4	1.1	37	40.1
50.8	8.8	2.9	0.8	35	34.5
60.8	8.3	2.7	0.7	36	34
66.8	7	1.9	1.2	34	32.7

350

351

352

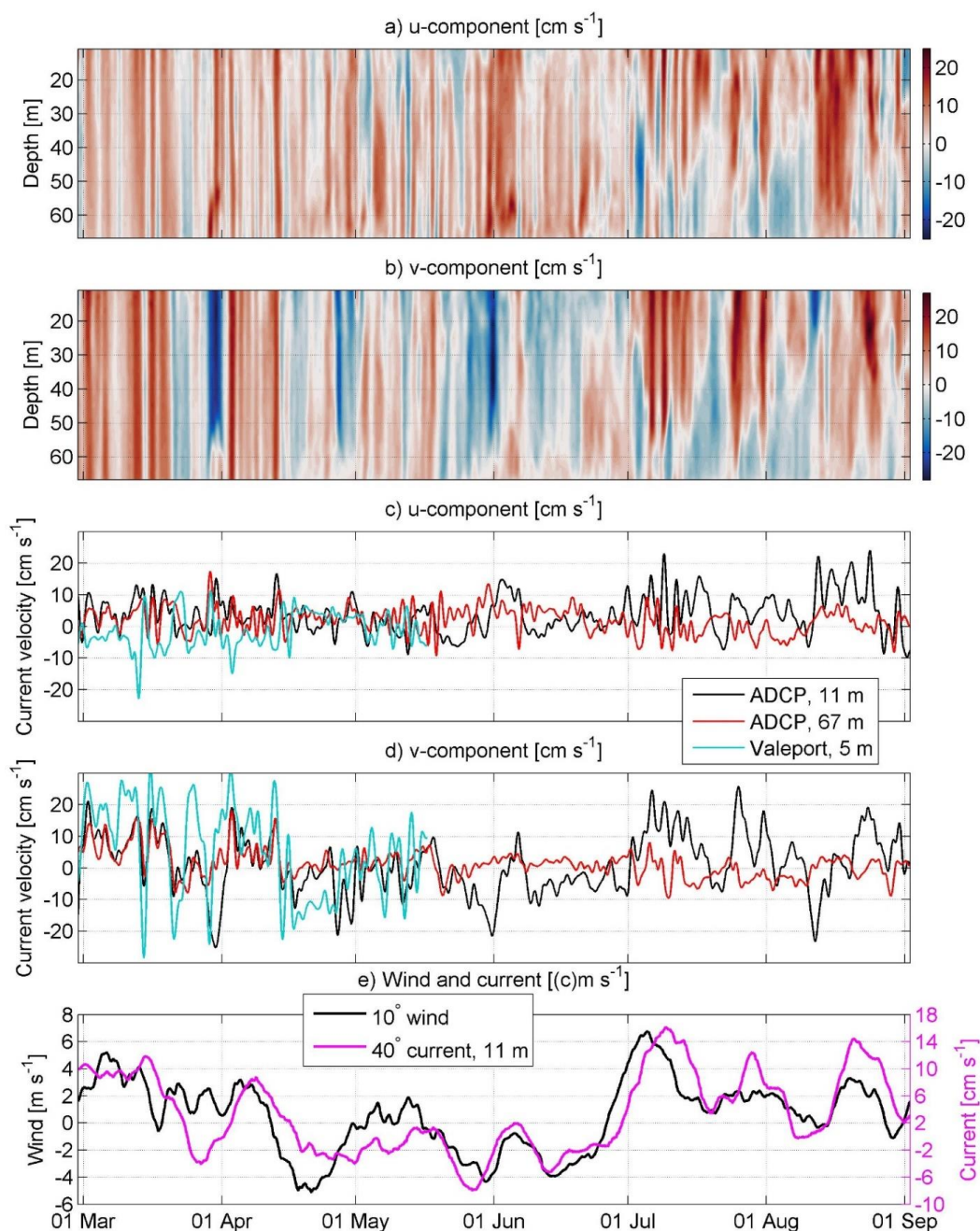
353

354

355

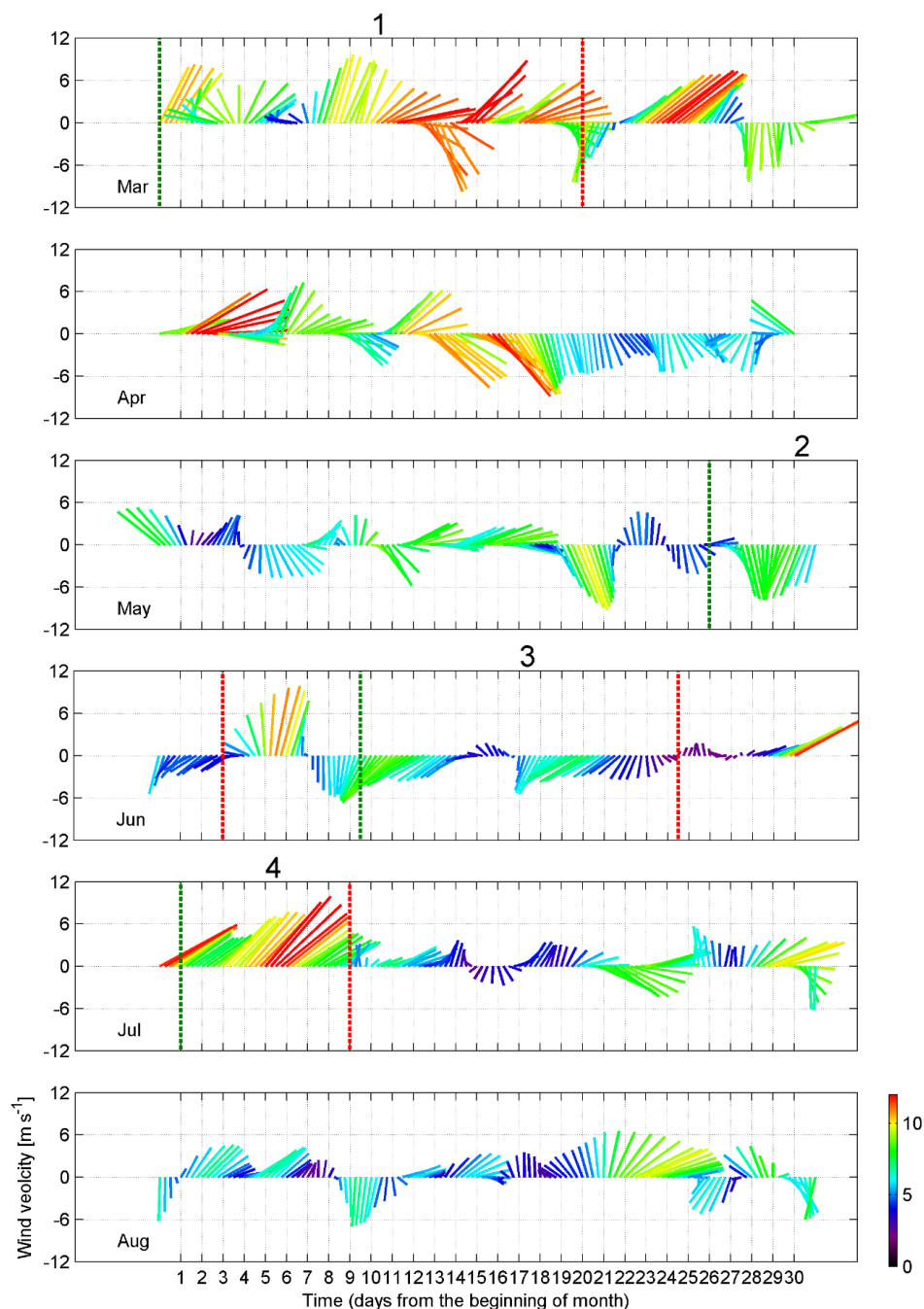
356

357



358

359 **Figure 3.** Temporal course of the low-pass filtered (36 h) current velocity *u*-component (positive eastward, a  
360 and c) and *v*-component (positive northward, b and d) in the water column (a, b); and in the upper (11 m depth)  
361 and deep layer (67 m depth, c, d) in the ADCP and Valeport locations in 2020 (Fig. 1). Low-pass filtered (10  
362 days) wind 10°-component and current 40°-component at 10 m depth in the ADCP location (e).

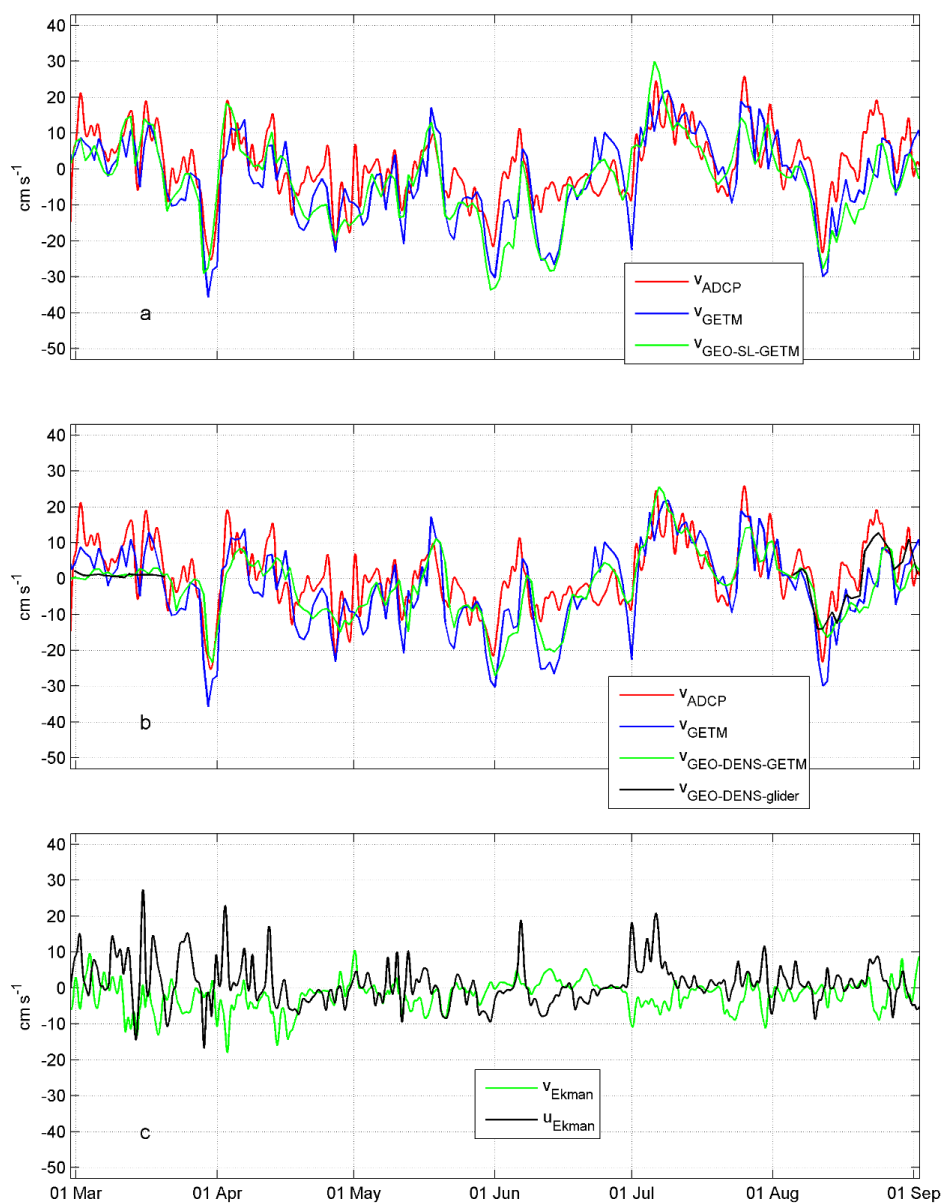


363

364 **Figure 4.** Time series of the 10-m level ERA5 wind data from 1 March to 31 August 2020. Four selected periods  
365 are shown: 1) prevailing southwesterly wind, 1–21 March; 2 and 3) prevailing northerly wind, 27 May–4 June  
366 and 10–25 June; 4) prevailing southwesterly wind, 2 July–10 July. The green dotted line marks the beginning  
367 and red dashed line marks the end of the period. Wind data were smoothed with a 36-h filter. Color scale shows  
368 wind speed in  $\text{m s}^{-1}$ .



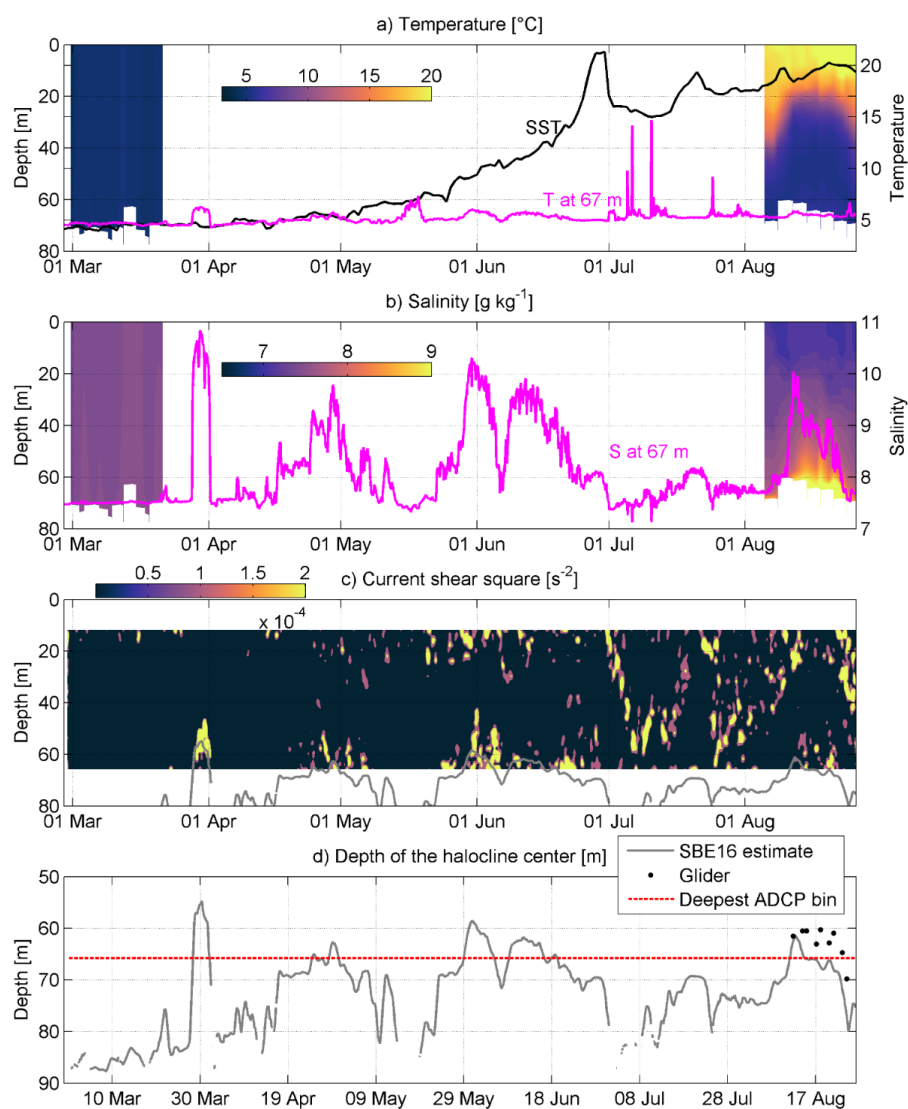
369



370  
371 **Figure 5.** Temporal courses of (a, b panel) current velocity  $v$ -component measured by ADCP ( $V_{\text{ADCP}}$ ), simulated  
372  $v$ -component ( $V_{\text{GETM}}$ ), estimated from the GETM sea level data ( $V_{\text{GEO-SL-GETM}}$ ), estimated from temperature and  
373 salinity data collected by glider ( $V_{\text{GEO-DENS-glider}}$ ), estimated from temperature and salinity data simulated by  
374 GETM at 11 m depth ( $V_{\text{GEO-DENS-GETM}}$ ). Mean Ekman current  $u$ -component and  $v$ -component ( $U_{\text{Ekman}}$  and  $V_{\text{Ekman}}$ )  
375 in the depth range 0–11 m (c). Time-series are shown from March to September 2020 at the ADCP location (see  
376 Fig. 1).



377



378

379 **Figure 6.** Temporal courses of temperature, salinity, current shear squared and halocline depth in the ADCP  
380 location from March to September 2020 (see Fig. 1b and c). (a) Temporal course of sea surface temperature  
381 (SST) and temperature at 67 m depth; temporal course of the vertical distribution of mean temperature in March  
382 and August calculated from glider data. (b) Temporal course of salinity at 67 m depth; temporal course of the  
383 vertical distribution of mean salinity in March and August calculated from glider data. Mean temperature and  
384 salinity profiles were calculated for each glider passing within the 3.7 km zonal window around the ADCP  
385 location. (c) Temporal course of the vertical distribution of current shear squared and depth of the halocline  
386 center (grey line). (d) Depth of halocline center, calculated from SBE16 data and in August from glider data.  
387 Depth of deepest ADCP bin is also shown (red dotted line).



### 388 3.2 Quasi-permanent circulation patterns

389 In the previous chapter, we demonstrated the importance of wind forcing and stratification for the  
390 currents. Next, we describe the current structure during the quasi-steady forcing periods. We have  
391 selected four periods of 8–21 days duration with relatively stable forcing (see Fig. 4) to analyze the  
392 mean measured and simulated flow structure in the ADCP and Valeport location (Fig. 7) and along the  
393 zonal section (Fig. 8). Likewise, we investigated the lateral simulated flow structures in the three  
394 forcing cases in three layers: upper layer (5 m), intermediate layer (40 m) and deep layer (110 m) (Figs.  
395 9–11).

396 The persistency of the currents was very high in all selected periods (Table 2). Only during the fourth  
397 period, the persistency was lower than 50% below the seasonal thermocline. Particularly high  
398 persistency (82–94%) occurred in the first and second periods. Thus, currents during the quasi-steady  
399 forcing have much higher persistency than overall of the time series (see Table 1).

400 Barotropic flow to the northeast prevailed throughout the water column at the ADCP location in the  
401 first period (1–21 March) when south-westerly wind prevailed (Fig. 7a and b). Even stronger mean  
402 current to the north-northwest was registered at 5 m depth at the Valeport location (Fig. 3c and d).  
403 Latter indicates the boundary effect near the Saaremaa Island. The current was directed along the coast.  
404 Mean flow was to the south in the upper layer during the second period (27 May–4 June) when  
405 northerly wind prevailed to the southeast below the thermocline and to the east below the halocline  
406 (Fig. 7e and f). In general, a similar current pattern occurred in the third period (10–25 June) when  
407 north-westerly wind prevailed (Fig. 7i and j). Due to relatively strong south-westerly wind forcing in  
408 the fourth period (2–10 July), flow to the northeast prevailed in the upper layer and to westerly  
409 directions below the thermocline (Fig. 7m and n).

410 In conclusion, a pattern typical for the downwelling event – current to the northeast along the boundary  
411 and towards the shore in the upper layer and seaward current to the southeast in the deep layer –  
412 occurred during southwesterly wind domination (Fig. 7f and j). The flow was to the south in the upper  
413 layer along the coast and onshore (east) in the deep layer, which is typical for the upwelling cell in the  
414 case of northerly winds (Fig. 7n). These vertical patterns of the current velocity were also well captured  
415 by the numerical model (Fig. 7g, k and o), although the magnitude of the mean simulated velocity  
416 occasionally deviated from the measured values. Likewise, the stronger mean measured current near  
417 the boundary at the Valeport location, was well reproduced by the model (Fig. 7b and c). Geostrophic  
418 velocities had a quite similar vertical structure compared to the measured velocities in all periods (Fig.  
419 7, third and fourth columns). Thus, currents were generally in geostrophic balance during the quasi-  
420 steady periods. The transition from one state to another has likely an ageostrophic nature, as wind is  
421 the main driver for the change.

422 Next, we analyze the vertical (Fig. 8) and horizontal (Fig. 9–11) structure of the mean meridional  
423 component of currents in the section along the latitude of the ADCP location (Fig. 1) and in the Eastern  
424 Gotland Basin using simulated current data. The current data are averaged within the same time  
425 windows with relatively stable wind forcing as analyzed above.

426 The structure of the meridional component of currents in the section is characterized by high spatial  
427 and temporal variability (Fig. 8). The unidirectional flow prevailed in most of the section down to the  
428 halocline or even deeper in the case of no thermal stratification and southwesterly winds (first period)  
429 (Fig. 8a). The northward current along the eastern boundary with a cross-coast extent of 10 km was  
430 especially strong. This strong boundary current was also registered by the Valeport (Fig. 3d). The  
431 strong maxima of the northward flow can be found between 20.5°–21.0° E, 18.6°–19.3° E and around





432 17.6° E. The strong southward flow prevailed between 21.0°–21.3° E, 19.4°–20.0° E, and 17.6°–18.6°  
433 E. Horizontal flow structure in the Eastern Gotland Basin consisted of the two stronger current zones  
434 above the halocline, northward current along the eastern boundary and southward current in the middle  
435 part (Fig. 9a and b). The two zones were connected with several cyclonic cells. The northward flow  
436 below the halocline (Fig. 9c) coincided with the flow in the upper layer in the Eastern Gotland Basin  
437 area but forced to the westward trajectory by bathymetry in the northern area.

438 The flow patterns were very similar in the following two periods (second and third) of prevailing  
439 northerly winds and the presence of thermocline. In both cases, the zonal scale of the southward flow  
440 around the ADCP location was 10–15 km (Fig. 8b and c). The flow did not extend to the eastern  
441 boundary, a narrow northward flow with a width of 5–10 km occurred along the coastal slope. The  
442 width of the southward flow near the western boundary of the section was about 30 km. In between,  
443 several circulation cells with zonal scales of 20–60 km can be distinguished in the cross-section (Fig.  
444 10a). The horizontal structure of the flow below the thermocline in the Eastern Gotland Basin revealed  
445 a strong southward current in the eastern part of the area in the second period (Fig. 10b). The current  
446 swirled, split into two branches and re-merged back to one in several locations. The southward flow  
447 below the thermocline coincided with the offshore branch in the upper layer in the central area of the  
448 basin (Fig. 10a and b). Sub-halocline flow revealed strongest northward current and strongest cyclonic  
449 cell in the Eastern Gotland basin among the selected periods (Fig. 10c).

450 The flow pattern in the case of strong southwesterlies dominance (fourth period) under stratified  
451 conditions revealed a strong northward current along both boundaries of the section (Fig. 8d). In  
452 between, the strong southward flow occurred in the surface layer. Similarly, to the northerly wind  
453 prevailing, complicated three-layer structure with variable horizontal patterns in the zonal scale of 20–  
454 60 km occurred. Flow to the southeast prevailed in the upper layer, except in the eastern boundary  
455 zone, where a strong northward downwelling related flow occurred (Fig. 11a), as also was observed in  
456 our ADCP mooring data (Fig. 7n). A strong current occurred also in the Irbe Strait towards the Gulf of  
457 Riga. Downwelling related flow along the eastern coast was also observed at 40 m depth (Fig. 11b). In  
458 the deep layer below the halocline, northward current along the eastern bottom slope and cyclonic cells  
459 in the Eastern Gotland Basin were observed (Fig. 11c).

460 Due to seasonality in forcing, variations in the circulation in this time scale can be expected. The  
461 boundary current in the eastern coast occurs year-round but is the strongest in winter. This is related to  
462 the wind regime: southwesterly winds prevail more in winter but are less frequent in spring and  
463 summer. The seasonal signal can be found in the whole section (Fig. 12). Well defined large cyclonic  
464 gyres in the Eastern Gotland Basin can be found in winter, while in spring and summer, the mean  
465 current structure is characterized by the smaller zonal scale features and weaker flow. However, it is  
466 noteworthy that the mean flow is to the north along the eastern coastal slope in all seasons.

467

### 468 3.3 Sub-halocline current

469 Cyclonic gyre was present below the halocline in the Eastern Gotland Basin in all selected periods  
470 (Figs. 9–11). The flow in this cyclonic system was especially strong along the eastern slope of the  
471 Eastern Gotland Basin. The northern branch of this circulation system is connected to the clearly  
472 distinguishable northward current. The position and magnitude of the current varied under different  
473 conditions. The current was stronger and meandered to west at the shallower area between Gotland and  
474 Fårö Deep in the case of northerly wind while it was slower, and the meandering did not occur in the  
475 case of southwesterly winds. To confirm the simulated cyclonic circulation in the Eastern Gotland



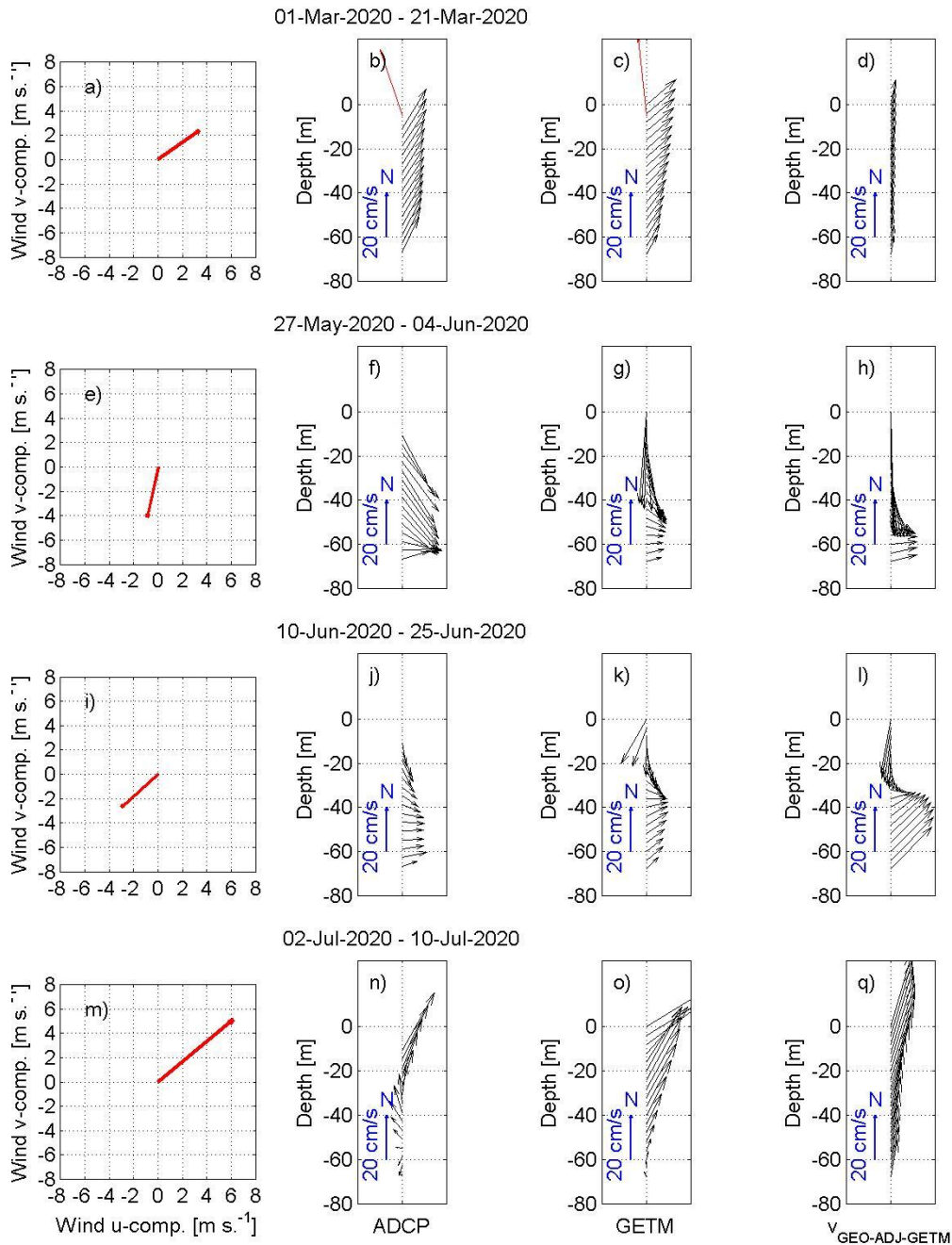
476 Basin and the northward flowing current towards the Northern Deep, the Argo float trajectory and the  
477 mean current field were plotted in the same time frame (Fig. 13a). The general features in the simulated  
478 mean currents and the Argo float trajectory agreed well. The Argo float first completed two circles  
479 (smaller and larger) in the Eastern Gotland Basin and then headed to the north. The float arrived and  
480 was recovered in the shallower area between the Fårö and Northern Deep. This sill is an important  
481 location for the deep layer water renewal in the Northern Baltic Proper (see bathymetry in Fig. 14), as  
482 this is the only remarkable passage to the north below 100 m depth. The sill is located slightly south of  
483 the selected section along the latitude of the ADCP deployment.

484 The flow to the north over the sill was concentrated in a narrow cell with a zonal scale of 5–6 km (Fig.  
485 15a). The flow was especially strong when northerly winds prevailed, e.g., in the second period from  
486 27 May to 4 June (Fig. 15b). The 2010–2020 mean density field sloped downward in the left (west) of  
487 the flow, typical for a gravity current (Fig. 15a–b). The meridional current velocity ( $C_T$ ) in the trench  
488 was mostly positive (northward) and in the range of 10–20  $\text{cm s}^{-1}$  during the study period in 2020 (Fig.  
489 15c). The  $C_T$  was reversed in the first half of July, which coincided with the strong southwesterly wind  
490 impulse (Fig. 4). The time series of  $C_T$  for 2010–2020 (Fig. 15d) revealed many reversal events, but  
491 the long-term mean meridional velocity was 10  $\text{cm s}^{-1}$  to the north. Reversals were most frequent in  
492 November–December when the monthly mean southward  $C_T$  was 6–7  $\text{cm s}^{-1}$  and rarer in March–May  
493 when monthly averages were in the range of 12–14  $\text{cm s}^{-1}$ . Thus, the deep layer water renewal in the  
494 Northern Baltic Proper is most active in the spring period and more restricted in late autumn–early  
495 winter. The best correlation ( $r^2=0.25$ ,  $p<10^{-100}$ ,  $n=3838$ ) between 10-day low-passed current velocity  
496 at the sill and wind was found with the wind from ENE (70°) with a delay of 6 days. This is another  
497 confirmation that prevailing southwesterly winds slow down or reverse the  $C_T$  and prevent deep water  
498 renewal in the Northern Baltic Proper.  
499

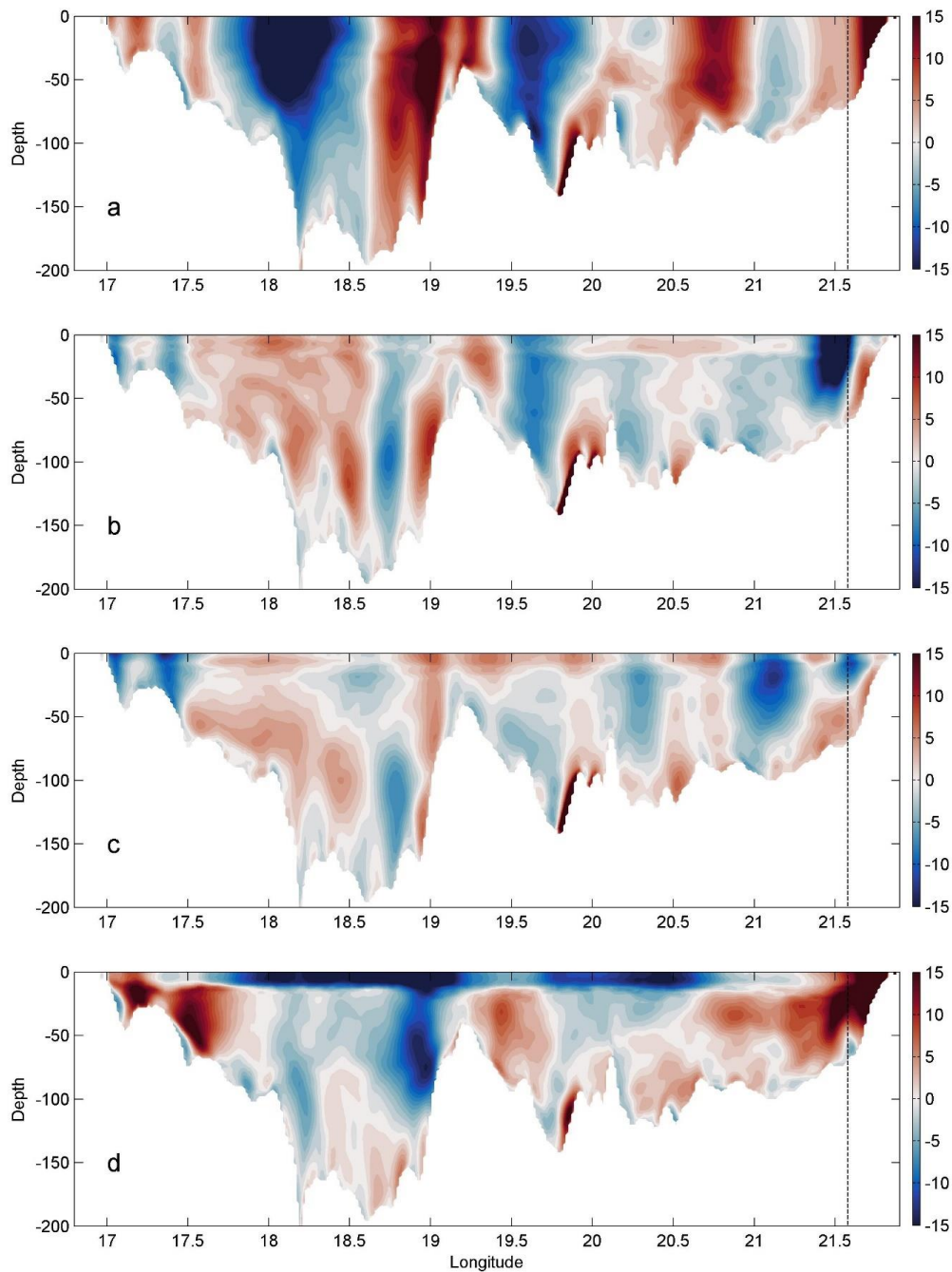
500 **Table 2.** Persistency (%) of the currents at the selected depths during the selected periods: 1 March to 21  
501 March (1); 27 May to 4 June (2); 10 June to 25 June (3); 2 July to 10 July (4) in 2020.

Period/ depth (m)	1	2	3	4
10.8	84.8	82	75.8	83.1
20.8	88.8	92.3	76.9	78.9
30.8	88.8	94	66.2	54.8
40.8	88.6	92.5	62.1	41.3
50.8	89.3	89.9	61.4	24
60.8	87.7	91.1	70.1	27.5
66.8	87.2	86.1	64.1	4.7

502  
503

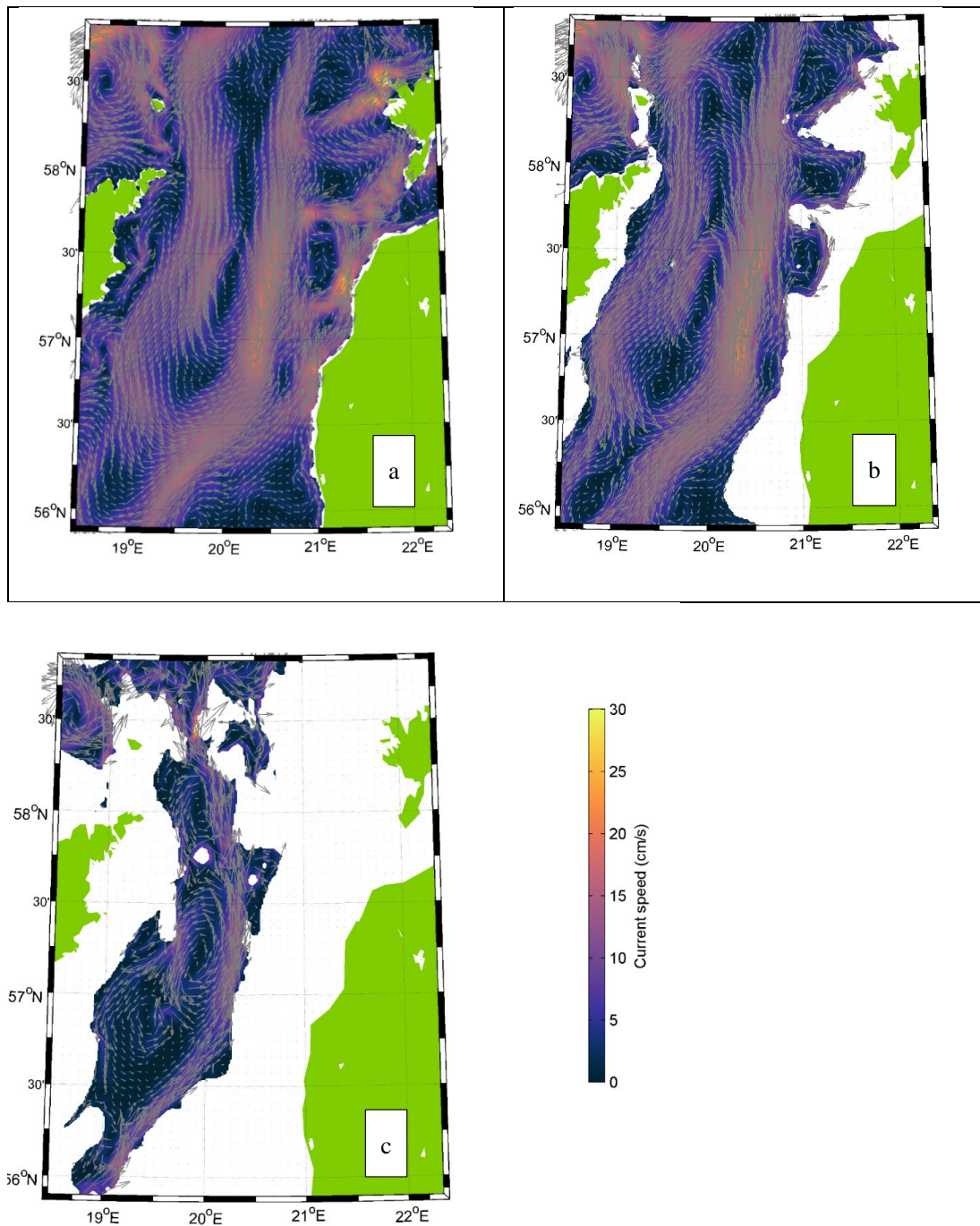


504  
 505 **Figure 7.** The mean resultant wind vectors (a, e, i, m), mean profiles of current velocity vectors calculated from  
 506 ADCP data (black arrows, b, f, j, n), mean current velocity vector based on Valeport data at 5 m depth (b, red  
 507 arrow), mean simulated current velocity vectors at the ADCP location (c, g, k, o) and at the Valeport location  
 508 (c, red arrow) are shown for selected periods (Fig. 4). On the right panels, mean adjusted geostrophic velocity  
 509 vectors  $V_{\text{GEO-ADJ-GETM}}$  (d, h, i, q) are shown.

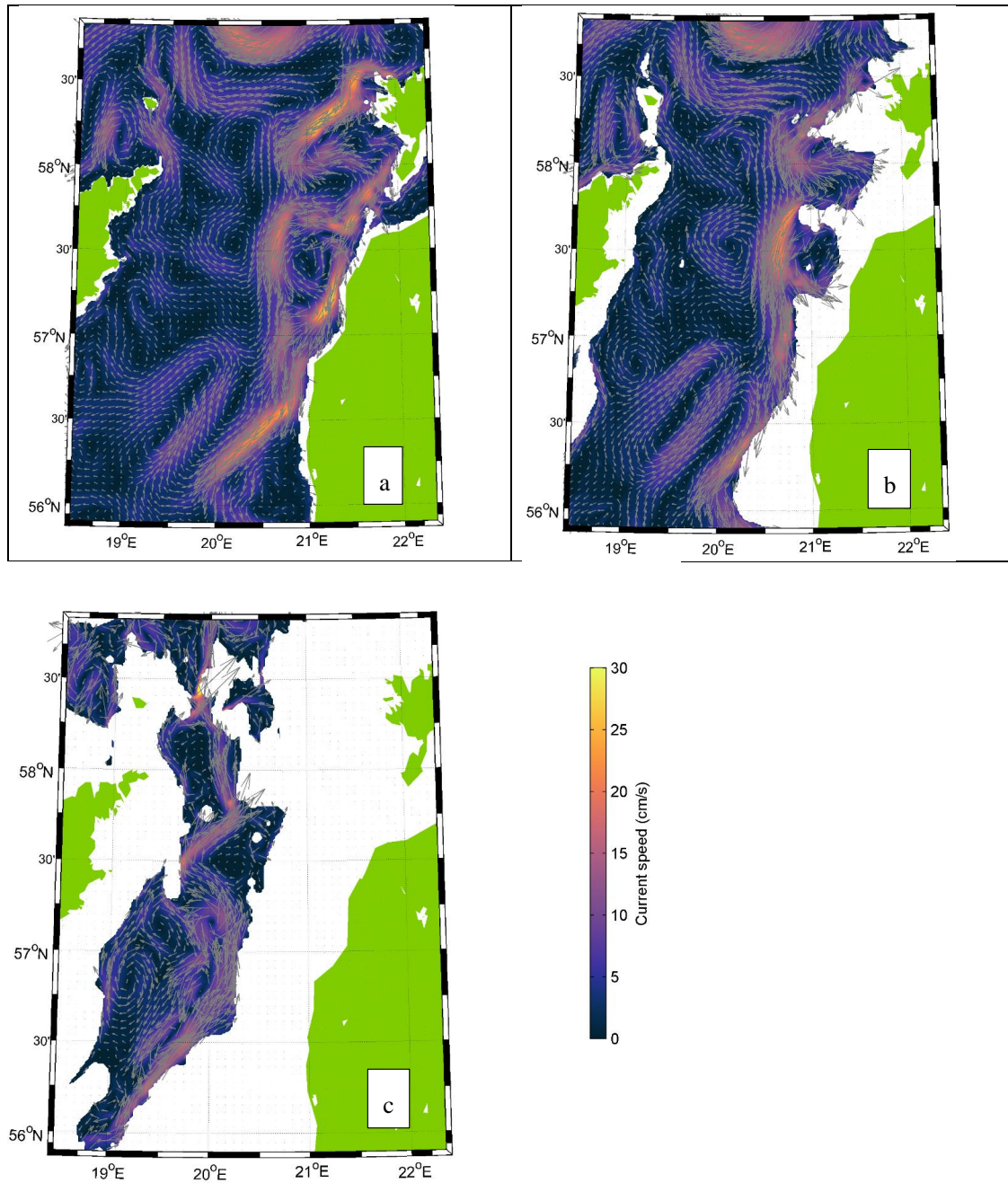


510  
511  
512  
513  
514

**Figure 8.** Vertical distribution of mean meridional current velocities for four selected periods (see Fig. 4) along the ADCP deployment latitude (Fig. 1b). Color scale displays meridional velocity (positive northward) in  $\text{cm s}^{-1}$ . Vertical dotted lines show the ADCP location.

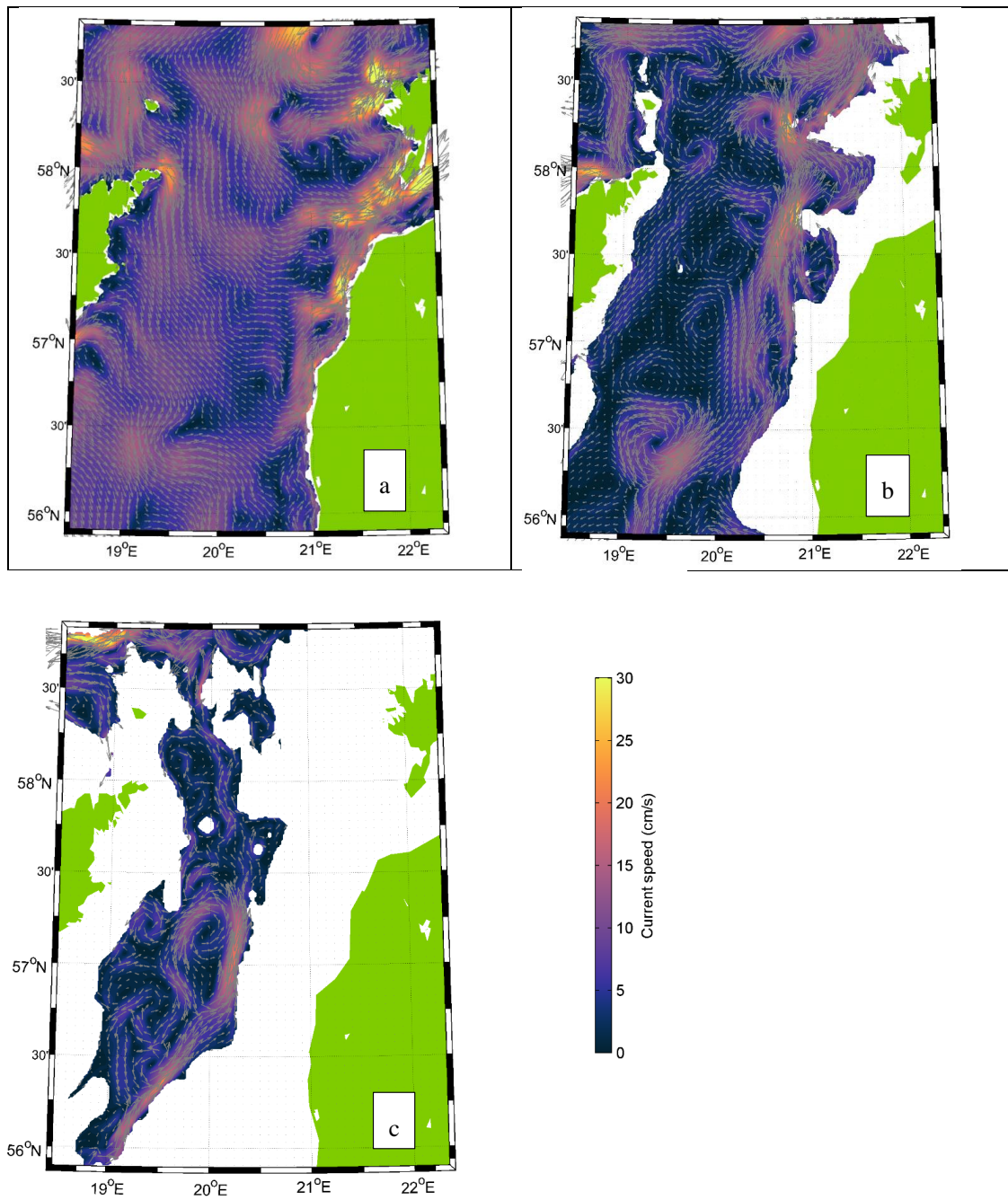


515  
516 **Figure 9.** Mean currents in the case of prevailing south-westerly winds from 1 March to 21 March 2020, without  
517 thermocline at 5 m depth (a), 40 m depth (b) and 110 m depth (c). Color scale shows current speed in  $\text{cm s}^{-1}$ .  
518

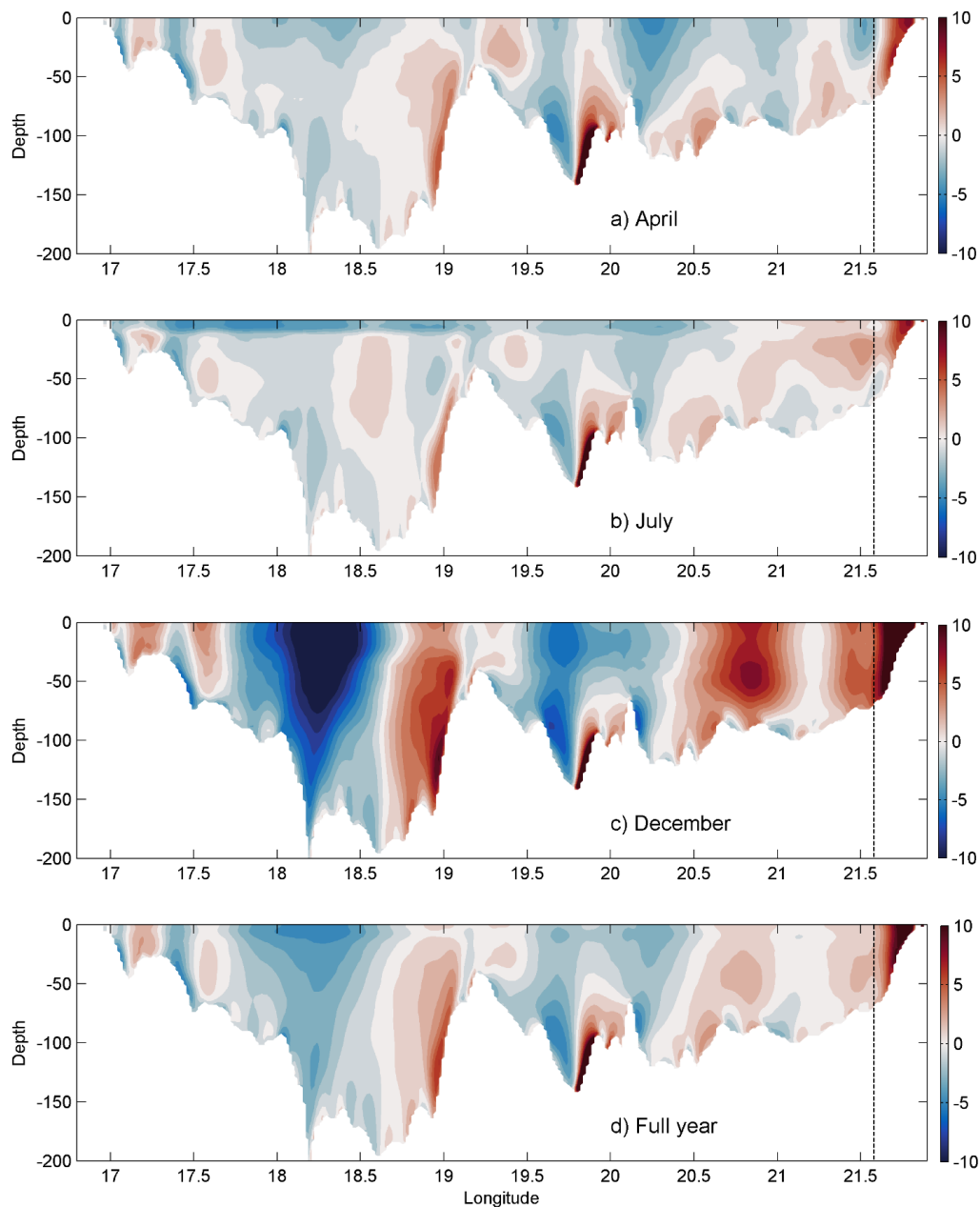


519  
520  
521  
522

**Figure 10.** Mean currents in the case of prevailing northerly winds from 27 May to 4 June 2020, with thermocline at 5 m depth (a), 40 m depth (b) and 110 m depth (c). Color scale shows current speed in  $\text{cm s}^{-1}$ .



523  
524 **Figure 11.** Mean currents in the case of prevailing south-westerly winds from 2 July to 7 July 2020, with  
525 thermocline at 5 m depth (a), 40 m depth (b) and 110 m depth (c). Color scale shows current speed in  $\text{cm s}^{-1}$ .  
526



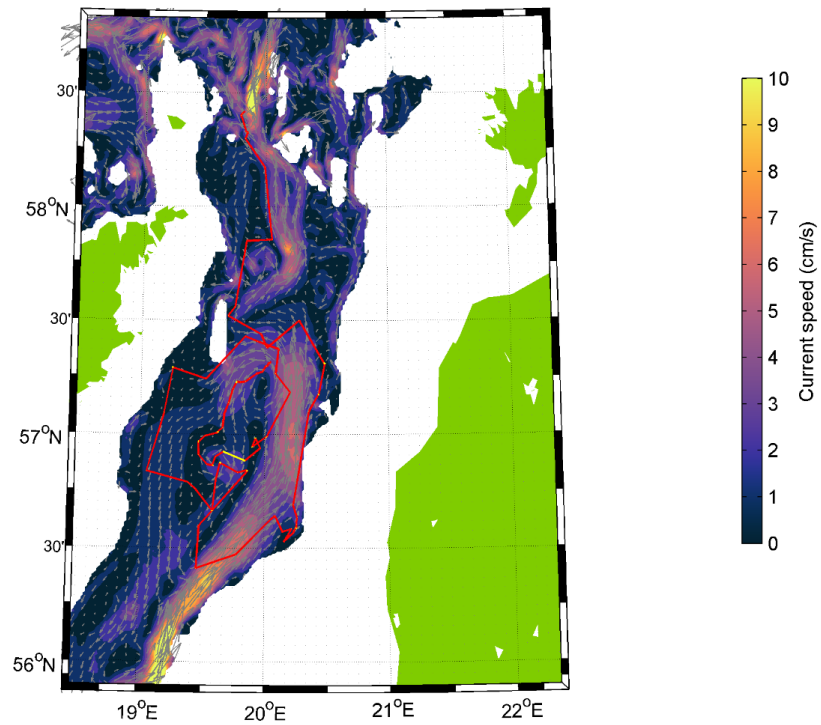
527  
528  
529  
530  
531  
532

**Figure 12.** Vertical distribution of monthly mean (April, July and December) and annual mean meridional velocities (positive northward) along the zonal section at ADCP latitude based on simulation data from September 2010 to August 2020. Color scale shows meridional velocity in  $\text{cm s}^{-1}$ . Vertical dotted lines show the ADCP location.



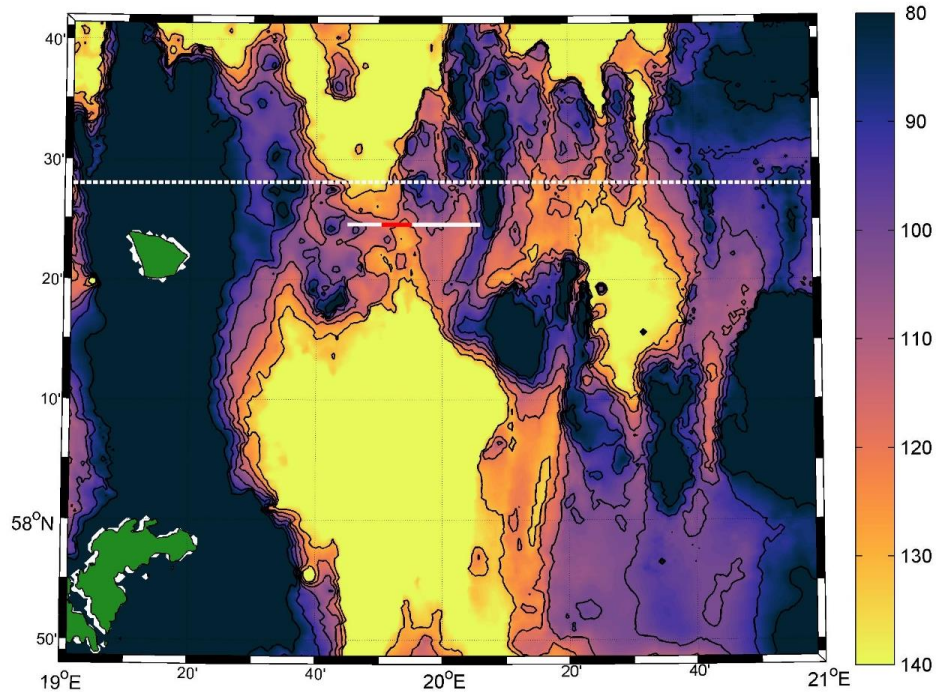


533  
534



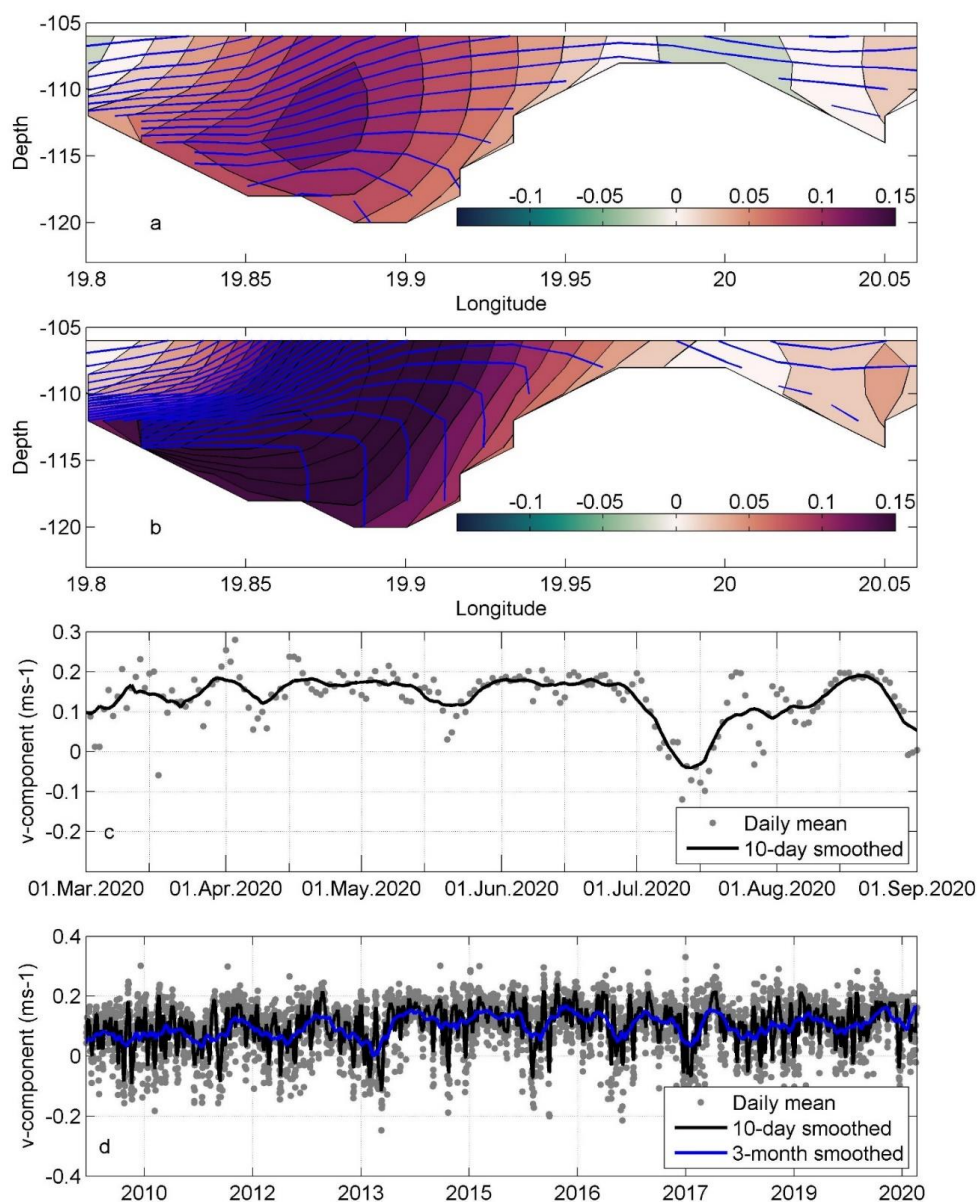
535  
536  
537  
538  
539  
540

**Figure 13.** Mean current field between 105–135 m depth based on simulation data and ARGO float trajectory during the period 15 August 2013–15 August 2014 in the deep layer (105–135 m, shown in red). Only one longer period occurred, when the float drifted on the surface (shown in white). Color scale shows current speed in  $\text{cm s}^{-1}$ .



541  
542  
543  
544

**Figure 14.** Bathymetry between Farø Deep and Northern Deep (see Fig. 1b). Color scale shows the depth in meters. White dashed line marks the section along the ADCP deployment latitude (Fig. 1b). White line marks the section in Fig. 15a, and red line indicates time-series calculation range for Fig. 15b–c.



545  
546 **Figure 15.** (a) mean simulated meridional current component  $v$  and density isolines at section below 105 m  
547 depth (the section location is shown as red line in Fig. 14) in 2010–2020, (b) mean meridional current component  
548  $v$  and density isolines at section below 105 m depth from 27 May to 4 June 2020 during a northerly wind impulse.  
549 In color scale contours with step of  $2 \text{ cm s}^{-1}$  show current  $v$ -component ( $\text{m s}^{-1}$ , positive northward) and blue  
550 lines show density isolines with a step of  $0.05 \text{ kg m}^{-3}$ . (c) time-series of  $v$  component below 105 m at the sill.  
551 Dots marks the daily mean and bold line 10-day smoothed  $v$ -component from March to September. (d) time-  
552 series of  $v$  component below 105 m at the sill. Dots marks the daily mean, bold black line 10-day smoothed and  
553 bold blue line 3-month smoothed  $v$ -component in the period 2010–2020.  
554



555

#### 556 **4 Discussion**

557 Moorings carrying ADCP and single-point current meter, and underwater glider surveys were applied,  
558 together with numerical modelling to investigate circulation in the Baltic Proper.

559 Strong linkage between the vertical location of the current shear maxima and the two pycnoclines was  
560 observed. The same finding was reported in the Gulf of Finland (Suhhova et al., 2018). The current  
561 shear maxima in the Gulf of Finland were related to the along-gulf estuarine circulation and its  
562 alterations. In the present case, the shear maxima were related to the currents along the basin axis and  
563 the coastal downwelling and upwelling circulation structures. The separation of the cross-shelf flow  
564 by a pycnocline has been documented in several other coastal systems (Davis, 2010; Gilcoto et al.,  
565 2017; Villaceros-Robineau et al., 2013).

566 Boundary current in the upper layer along the eastern coast was observed. The current was well  
567 correlated with the wind. The wind regime in the area is the combination of the global circulation and  
568 specific direction-dependent boundary-layer effects, which results in domination of winds along the  
569 axis of the Baltic Proper (Soomere & Keevallik, 2001). Along-axis wind causes the Ekman current  
570 (Ekman, 1905) to the right from wind direction in the upper layer, i.e., a flow across the basin axis.  
571 The resulting convergence (divergence) in the case of southwesterly (northerly) winds at the eastern  
572 coast causes across-axis sea level gradient and the upper pycnocline inclination, which in turn cause  
573 horizontal pressure gradient, and results in a geostrophic flow to the north (south) in the upper layer.  
574 Boundary currents forced by the pressure gradient caused by wind-driven divergence/convergence are  
575 common in coastal systems (Berden et al., 2020; Longdill et al., 2008; H. Wu et al., 2013). The  
576 geostrophic current velocity is well agreed with the total current velocity profiles. Thus, the current  
577 along the boundary was generally in the geostrophic balance, but across-shore ageostrophic flow  
578 created preconditions for this geostrophic coastal current.

579 Circulation rapidly reacted to the wind forcing. Persistency of the current for 6 months was rather low  
580 (30–40%) due to variability in the wind forcing. The estimated persistency from long-term numerical  
581 simulations data in the same area above the halocline was 70–80% in 1981–2004 (Meier, 2007) but  
582 around 30–40% in the upper layer in 1958–2007 (Jędrasik & Kowalewski, 2019). However, the quasi-  
583 steady circulation patterns detected under different wind and stratification conditions were high-  
584 persistent, mostly >75%.

585 The mean cyclonic circulation in the upper layer of the Baltic Proper has been reported by many  
586 modeling studies (Hinrichsen et al., 2018; Jedrasik et al., 2008; Jędrasik & Kowalewski, 2019; Meier,  
587 2007; Placke et al., 2018). However, the magnitude of the long-term mean circulation patterns had a  
588 considerably lower magnitude than the quasi-steady circulation structures presented in this study.  
589 Likewise, the current direction of quasi-steady patterns varied and differed considerably from the long-  
590 term mean. The circulation structures in this timescale also differ from the long-term mean because of  
591 seasonal and inter-annual variations in the forcing. The cyclonic circulation and the eastern boundary  
592 current towards the north in the upper layer is stronger in autumn and winter, as noted by previous  
593 simulations (Jędrasik & Kowalewski, 2019), when strong southwesterly winds are more frequent  
594 (Soomere & Keevallik, 2001). Quasi-steady circulation patterns were characterized by complicated  
595 lateral vortices with the zonal scale of 20–60 km. The richness of vortical structures has been suggested  
596 by several numerical modelling studies (Dargahi, 2019; Zhurbas et al., 2021). In-situ measurements



597 are needed to verify the existence of the vortices and to characterize their effect on the physical and  
598 biogeochemical fields in more detail.

599 Two quasi-permanent circulation features were detected in the deep layer. Cyclonic gyre was present  
600 below the halocline in the Eastern Gotland Basin, with the strongest flow along the eastern slope, which  
601 has been documented by in-situ measurements earlier (Hagen & Feistel, 2004; Hagen & Feistel, 2007).  
602 The northern branch of the Eastern Gotland Basin current is connected to the quasi-steady northward-  
603 flowing current towards narrow Fårö sill between the Fårö and Northern Deep. The width of the current  
604 was mostly 10–30 km, but only 5 km at the sill. The mean northward component of the current was 10  
605  $\text{cm s}^{-1}$ , which can be explained by the mean density structure (Fig. 15a) and is typical for the gravity  
606 current in a channel (Zhurbas et al., 2012). This current is an important deeper limb of the Baltic haline  
607 conveyor belt (Döös et al., 2004). The current was stronger in the case of northerly winds and weaker  
608 during southwesterly wind prevailing. This is typical behavior of the estuarine circulation: up-estuary  
609 wind causes weakening or reversal of the deep layer current and down-estuary wind intensification of  
610 the estuarine current (Geyer & MacCready, 2014) as observed in the Gulf of Finland (Liblik et al.,  
611 2013; Lilover et al., 2017; Suhhova et al., 2018) and several other estuaries (e.g. Giddings &  
612 MacCready, 2017; Scully, 2016). In the case of northerly wind, the vertical and horizontal density  
613 gradient in the Fårö sill was much stronger (Fig. 15b) than the mean gradient in 2010–2020 (Fig. 15a)  
614 according to the simulation. Note that on the right-hand flank, the isopycnals are vertical (Fig. 15b). A  
615 similar structure of the gravity current has been measured by acoustic profiling in the Western Baltic  
616 (Umlauf et al., 2009). The current to the north and potentially the deep layer water renewal in the  
617 Northern Baltic Proper is more intense in March–May when southwesterly winds are less frequent, and  
618 the current is weakest in November–December. If the water that overflows the Fårö sill is dense  
619 enough, it occupies the Northern Deep bottom layers, and the old, oxygen-depleted bottom water is  
620 lifted and advected to the Gulf of Finland, as observed during high Major Baltic Inflow activity (Liblik  
621 et al., 2018). If the overflow has a lower density compared to the deep layer waters in the Northern  
622 Deep, it does not dive to the bottom but stays as a buoyant layer.

623

624 The most favorable wind for the up-estuary deep layer advection in the Gulf of Finland is from the  
625 northeast (Elken et al., 2003). Thus, northerly winds support deep water renewal and strengthening of  
626 the stratification all the way from the Gotland Deep to the Gulf of Finland. The deep layer currents are  
627 quite well covered by observations in the Gulf of Finland (Lilover et al., 2017; Rasmus et al., 2015;  
628 Suhhova et al., 2018). However, observations are lacking from the Gotland Deep to the entrance of the  
629 Gulf of Finland. The only in-situ record about the feature between Gotland and Northern Deep is the  
630 Argo float track. The Argo trajectory supported our suggestion about the existence of the sub-halocline  
631 current to the north. Our simulations suggested that the strength and position of the current did depend  
632 on the wind forcing. Observations and simulation results at the channel-like topographic constriction,  
633 Slupsk Furrow, in the southern Baltic have shown that the meandering of the gravity current is strongly  
634 affected by the bottom topography and wind-forcing (Zhurbas et al., 2012). ADCP measurements are  
635 needed to understand the behavior of the sub-halocline current better.

636 Overall, simulated currents quite well agree with the ADCP measurements in the upper layer. However,  
637 the meridional component of the simulated current ( $V_{\text{GETM}}$ ) was biased (Fig. 5a). The mean  $V_{\text{ADCP}}$  was  
638  $1.1 \text{ cm s}^{-1}$ , but the mean  $V_{\text{GETM}}$  was  $-3.2 \text{ cm s}^{-1}$  at 10 m depth during the study period. Such bias could  
639 not be found in the deep layer. Flow to the north was often weaker compared to measurements ( $V_{\text{ADCP}}$ ),  
640 and flow to the south was stronger than observed by the ADCP in the upper layer. A similar tendency  
641 can be found in a comparison of the ADCP measurements and simulation results in the Gulf of Finland

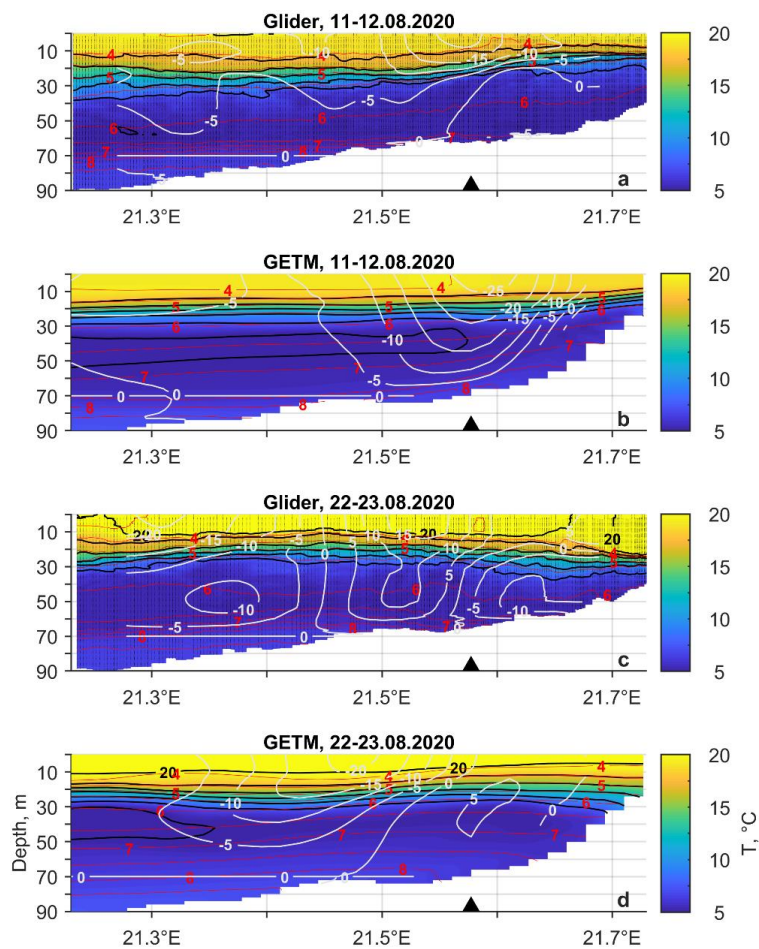


642 (Suhhova et al., 2015). Near the right-hand side coast (looking up-estuary, i.e., to the east in the Gulf  
643 of Finland), the down-estuary flow was stronger and more frequent in the simulation compared to the  
644 measurements (see their Fig. 2). Interestingly, a similar bias was detected in the deep layer at the eastern  
645 flank of the Gotland Deep at 204 m depth (Placke et al., 2018). Four different models considerably  
646 underestimated (Placke et al., 2018) the mean flow to the north derived from observations (Hagen &  
647 Feistel, 2004). The first possible explanation for the bias could be the smaller width of the boundary  
648 current. Indeed, the mean flow towards north in 2010–2020 was stronger in the east from the ADCP  
649 location (Fig. 12). The second possible source for the discrepancy could be related to the performance  
650 of simulation of ageostrophic or geostrophic flow. We will discuss this further in the next section.

651 Quite large discrepancies between the simulation and the measurements occurred in June. In the first  
652 half of the month, simulation was biased to the south, but in the second half, a bias to the north can be  
653 seen (Fig. 5a). In both cases, the geostrophic current seems to play an important role in the discrepancy.  
654 Strong simulated  $V_{\text{GEO-DENS-GETM}}$  to the south (north) occurred in the first (second) part of June. In  
655 August, the simulation did not capture the strongest flow event to the north on 21–24 August (Fig. 5a).  
656 At the same period, much lower values of the  $V_{\text{GEO-DENS-GETM}}$  compared to the  $V_{\text{GEO-DENS-glider}}$  can be  
657 seen. These signs suggest, first, that the isopycnals in the model react to the forcing more rapidly than  
658 in the sea. Secondly, there is a bias in the across/slope seasonal thermocline inclination. Likely, the  
659 thermocline is tilted more towards the surface near the coast in the model than in the sea. We next  
660 evaluate the measured (by glider) and simulated temperature, salinity and geostrophic velocity fields  
661 on 11–12 August and on 22–23 August.

662 Surface layer geostrophic velocity in the simulation agrees well with the estimates from the glider data  
663 on 11–12 August (Fig. 16a–b). Though, the glider observations reveal sharper thermocline inclination  
664 than the simulation. Discrepancies in the temperature, density, and geostrophic current fields on 22–  
665 23 August are much larger (Fig. 16c–d). Glider observations revealed the thermocline depressed down  
666 near the coast, which is typical for a downwelling. The inclination in the thermocline caused strong  
667 geostrophic flow to the north in the location of ADCP (Fig. 16c). Homogenous mixed layer reached  
668 down to 22 m depth at the easternmost end of the section. Such an inclination, well defined  
669 homogenous layer and geostrophic current to the north at the ADCP location was not revealed by the  
670 simulation (Fig. 16c). Thus, we can conclude that the bias in the boundary current simulation could be  
671 related to the inaccuracy of reproducing the temperature and salinity fields and the resulting  
672 geostrophic component of currents. We are not going into further details of this problem here, as it is  
673 out of the focus of the present work. However, conclusions of the simulation studies that have focused  
674 on the long-term mean current fields in the upper layer, but did not validate simulations with direct  
675 current observations, should be taken carefully, as the magnitude of the long-term residual current is  
676 very small compared to the magnitude of the currents during the quasi-steady states. We suggest a  
677 dedicated study involving numerous current profiling records should be conducted to track down the  
678 causes of the discrepancies between observations and simulations.

679



680

681 **Figure 16.** Temperature (color contours), density isolines (red lines), relative geostrophic current (white lines)  
682 based on glider observations and GETM simulation on 11–12 August and 22–23 August 2020.

683

684

685



## 686            **5 Conclusions**

687    A strong link between the existence and location of the two pycnoclines and the current structure was  
688    observed. Boundary current was observed in the upper layer along the eastern coast of the Baltic  
689    Proper. The current was mainly in geostrophic balance, but across-shore Ekman transport created  
690    preconditions for the geostrophic coastal current. The boundary current rapidly reacted to the changes  
691    in the wind forcing that is reflected in a relatively low persistency of currents (30–40%) in the whole  
692    water column during the 6-month measurement period. However, the quasi-steady circulation patterns  
693    formed under the certain wind and stratification conditions were high-persistent (mostly >80%) and  
694    generally in the geostrophic balance.

695    The sub-halocline, quasi-steady northward (towards Fårö sill) gravity current with a width of 10–30  
696    km was detected by the simulation. The finding was supported by the Argo float displacement data.  
697    This important deeper limb of the Baltic Sea haline conveyor belt is stronger in the case of northerly  
698    winds and weaker during south-westerlies. More detailed studies of the dynamics and water properties  
699    of this current are essential to understand the renewal process of deep layer waters in the Northern  
700    Baltic Proper and in the Gulf of Finland.

701    Generally, the structure of boundary current was well reproduced by the GETM. However, the  
702    meridional component of the simulated current was biased southward. Further investigations of the  
703    current regimes in various locations during the periods of quasi-steady forcing could help to reveal the  
704    causes of the discrepancy.

705    *Code availability.* Scripts to analyze the results are available upon request. Please contact Taavi Liblik.

706    *Author contributions.* TL led the analyses of the data and writing of the paper with contributions from  
707    GV, JL, UL, KS and MJL. TL was responsible for the measurements and data processing, and GV for  
708    the modelling activities. KS processed the glider data.

709

710    *Competing interests.* The authors declare that they have no conflict of interests.

711

712    *Acknowledgements.* We would like to thank our colleagues and research vessels Salme crew for all the  
713    support in measurements and operations at sea. The computing time from high-performance computing  
714    center at Tallinn University of Technology and University of Tartu are gratefully acknowledged.  
715    GETM community at Leibniz Institute of Baltic Sea Research are gratefully acknowledged for  
716    maintaining and developing the code.

717

718    *Financial support.* This work was supported by the Estonian Research Council grant PRG602.  
719    Collection of the data was financially supported by the European Regional Development Fund within  
720    National Programme for Addressing Socio-Economic Challenges through R&D (RITA). Infrastructure  
721    assets used in the current study are part of the JERICO infrastructure and supported by the JERICO-  
722    S3 project under the European Union's Horizon 2020 research and innovation programme with grant  
723    number 871153.





724

725

726 **References**

- 727 Berden, G., Charo, M., Möller, O. O., & Piola, A. R. (2020). Circulation and Hydrography in the  
728 Western South Atlantic Shelf and Export to the Deep Adjacent Ocean: 30°S to 40°S. *Journal of*  
729 *Geophysical Research: Oceans*, 125(10), e2020JC016500.  
730 <https://doi.org/10.1029/2020JC016500>
- 731 Book, J., Perkins, H., Signell, R., & Wimbush, M. (2007). The Adriatic Circulation Experiment  
732 winter 2002/2003 mooring data report: a case study in ADCP data processing. In *U.S. Naval*  
733 *Res. Lab. Stennis Space Center*.
- 734 Burchard, H., & Bolding, K. (2002). *GETM – a general estuarine transport model. Scientific*  
735 *Documentation. Technical report EUR 20253 en. In: Tech. Rep. European Commission*.
- 736 Carstensen, J., Andersen, J. H., Gustafsson, B. G., & Conley, D. J. (2014). Deoxygenation of the  
737 baltic sea during the last century. *Proceedings of the National Academy of Sciences of the*  
738 *United States of America*, 111(15), 5628–5633. <https://doi.org/10.1073/pnas.1323156111>
- 739 Csanady, G. T. (1981). Circulation in the Coastal Ocean. *Advances in Geophysics*, 23(C), 101–183.  
740 [https://doi.org/10.1016/S0065-2687\(08\)60331-3](https://doi.org/10.1016/S0065-2687(08)60331-3)
- 741 Dargahi, B. (2019). Dynamics of vortical structures in the Baltic Sea. *Dynamics of Atmospheres and*  
742 *Oceans*, 88, 101117. <https://doi.org/10.1016/j.dynatmoce.2019.101117>
- 743 Davis, R. E. (2010). On the coastal-upwelling overturning cell. *Journal of Marine Research*, 68(3–4),  
744 369–385. <https://doi.org/10.1357/002224010794657173>
- 745 Döös, K., Meier, H. E. M., & Döscher, R. (2004). The Baltic Haline Conveyor Belt or The  
746 Overturning Circulation and Mixing in the Baltic. *AMBIO: A Journal of the Human*  
747 *Environment*, 33(4), 261–266. <https://doi.org/10.1579/0044-7447-33.4.261>
- 748 Ekman, V. W. (1905). On the influence of the earth's rotation on ocean currents. *Arkiv. Mat., Astron.*  
749 *Fys.*, 11, 1–52.
- 750 Elken, J., Raudsepp, U., & Lips, U. (2003). On the estuarine transport reversal in deep layers of the  
751 Gulf of Finland. *Journal of Sea Research*, 49(4), 267–274. [https://doi.org/10.1016/S1385-](https://doi.org/10.1016/S1385-1101(03)00018-2)  
752 [1101\(03\)00018-2](https://doi.org/10.1016/S1385-1101(03)00018-2)
- 753 Geyer, W. R., & MacCready, P. (2014). The Estuarine Circulation. *Annual Review of Fluid*  
754 *Mechanics*, 46(1), 175–197. <https://doi.org/10.1146/annurev-fluid-010313-141302>
- 755 Giddings, S. N., & MacCready, P. (2017). Reverse Estuarine Circulation Due to Local and Remote  
756 Wind Forcing, Enhanced by the Presence of Along-Coast Estuaries. *Journal of Geophysical*  
757 *Research: Oceans*, 122(12), 10184–10205. <https://doi.org/10.1002/2016JC012479>
- 758 Gilcoto, M., Largier, J. L., Barton, E. D., Piedracoba, S., Torres, R., Graña, R., Alonso-Pérez, F.,  
759 Villaceros-Robineau, N., & de la Granda, F. (2017). Rapid response to coastal upwelling in a



- 760 semienclosed bay. *Geophysical Research Letters*, 44(5), 2388–2397.  
761 <https://doi.org/10.1002/2016GL072416>
- 762 Golenko, M., Krayushkin, E., & Lavrova, O. (2017). Современные проблемы дистанционного  
763 зондирования Земли из космоса. *Current Problems in Remote Sensing of the Earth from*  
764 *Space.*, 280–296. <https://doi.org/10.21046/2070-7401-2017-14-7-280-296>
- 765 Hagen, E., & Feistel, R. (2004). Observations of low-frequency current fluctuations in deep water of  
766 the Eastern Gotland Basin/Baltic Sea. *Journal of Geophysical Research: Oceans*, 109(C3).  
767 <https://doi.org/10.1029/2003JC002017>
- 768 Hagen, Eberhard, & Feistel, R. (2007). Synoptic changes in the deep rim current during stagnant  
769 hydrographic conditions in the Eastern Gotland Basin, Baltic Sea. *Oceanologia*, 49(2), 185–208.
- 770 Hersbach, H., Bell, B., Berrisford, P., Hirahara, S., Horányi, A., Muñoz-Sabater, J., Nicolas, J.,  
771 Peubey, C., Radu, R., Schepers, D., Simmons, A., Soci, C., Abdalla, S., Abellan, X., Balsamo,  
772 G., Bechtold, P., Biavati, G., Bidlot, J., Bonavita, M., ... Thépaut, J.-N. (2020). The ERA5  
773 global reanalysis. *Quarterly Journal of the Royal Meteorological Society*, 146(730), 1999–2049.  
774 <https://doi.org/10.1002/QJ.3803>
- 775 Hinrichsen, H. H., von Dewitz, B., & Dierking, J. (2018). Variability of advective connectivity in the  
776 Baltic Sea. *Journal of Marine Systems*, 186, 115–122.  
777 <https://doi.org/10.1016/j.jmarsys.2018.06.010>
- 778 Holtermann, P. L., Prien, R., Naumann, M., Mohrholz, V., & Umlauf, L. (2017). Deepwater  
779 dynamics and mixing processes during a major inflow event in the central Baltic Sea. *Journal of*  
780 *Geophysical Research: Oceans*, 122(8), 6648–6667. <https://doi.org/10.1002/2017JC013050>
- 781 Jakobsen, F., Hansen, I. S., Ottesen Hansen, N. E., & Østrup-Rasmussen, F. (2010). Flow resistance  
782 in the Great Belt, the biggest strait between the North Sea and the Baltic Sea. *Estuarine, Coastal*  
783 *and Shelf Science*, 87(2), 325–332. <https://doi.org/10.1016/j.ecss.2010.01.014>
- 784 Janssen, F., Schrum, C., & Backhaus, J. O. (1999). A climatological data set of temperature and  
785 salinity for the Baltic Sea and the North Sea. *Deutsche Hydrographische Zeitschrift*, 51(S9), 5–  
786 245. <https://doi.org/10.1007/BF02933676>
- 787 Jedrasik, J., Cieřlikiewicz, W., Kowalewski, M., Bradtke, K., & Jankowski, A. (2008). 44 Years  
788 Hindcast of the sea level and circulation in the Baltic Sea. *Coastal Engineering*, 55(11), 849–  
789 860. <https://doi.org/10.1016/j.coastaleng.2008.02.026>
- 790 Jędrasik, J., & Kowalewski, M. (2019). Mean annual and seasonal circulation patterns and long-term  
791 variability of currents in the Baltic Sea. *Journal of Marine Systems*, 193, 1–26.  
792 <https://doi.org/10.1016/j.jmarsys.2018.12.011>
- 793 Jönsson, B., Döös, K., Nycander, J., & Lundberg, P. (2008). Standing waves in the Gulf of Finland  
794 and their relationship to the basin-wide Baltic seiches. *Journal of Geophysical Research*,  
795 113(C3), C03004. <https://doi.org/10.1029/2006JC003862>
- 796 Krayushkin, E., Lavrova, O., & Strochkov, A. (2019). Application of GPS/GSM Lagrangian mini-  
797 drifters for coastal ocean dynamics analysis. *Russian Journal of Earth Sciences*, 19(1).



- 798 <https://doi.org/10.2205/2018ES000642>
- 799 Leppäranta, M., & Myrberg, K. (2009). Circulation. In *Physical Oceanography of the Baltic Sea* (pp.  
800 131–187). Springer Berlin Heidelberg. [https://doi.org/10.1007/978-3-540-79703-6\\_5](https://doi.org/10.1007/978-3-540-79703-6_5)
- 801 Liblik, T., Laanemets, J., Raudsepp, U., Elken, J., & Suhhova, I. (2013). Estuarine circulation  
802 reversals and related rapid changes in winter near-bottom oxygen conditions in the Gulf of  
803 Finland, Baltic Sea. *Ocean Science*, 9, 917–930.
- 804 Liblik, T., Naumann, M., Alenius, P., Hansson, M., Lips, U., Nausch, G., Tuomi, L., Wesslander, K.,  
805 Laanemets, J., & Viktorsson, L. (2018). Propagation of Impact of the Recent Major Baltic  
806 Inflows From the Eastern Gotland Basin to the Gulf of Finland. *Frontiers in Marine Science*, 5,  
807 222. <https://doi.org/10.3389/fmars.2018.00222>
- 808 Liblik, T., Väli, G., Lips, I., Lilover, M.-J., Kikas, V., & Laanemets, J. (2020). The winter  
809 stratification phenomenon and its consequences in the Gulf of Finland, Baltic Sea. *Ocean*  
810 *Science*, 16, 1475–1490.
- 811 Lilover, M.-J., Elken, J., Suhhova, I., & Liblik, T. (2017). Observed flow variability along the  
812 thalweg, and on the coastal slopes of the Gulf of Finland, Baltic Sea. *Estuarine, Coastal and*  
813 *Shelf Science*, 195, 23–33.
- 814 Lilover, M.-J., Pavelson, J., & Kõuts, T. (2011). Wind forced currents over the shallow naissaar Bank  
815 in the Gulf of Finland. In *Boreal environment research* (Vol. 16).
- 816 Longdill, P. C., Healy, T. R., & Black, K. P. (2008). Transient wind-driven coastal upwelling on a  
817 shelf with varying width and orientation. *New Zealand Journal of Marine and Freshwater*  
818 *Research*, 42(2), 181–196. <https://doi.org/10.1080/00288330809509947>
- 819 Macdonald, A. M. (1998). The global ocean circulation: a hydrographic estimate and regional  
820 analysis. *Progress in Oceanography*, 41(3), 281–382. [https://doi.org/10.1016/S0079-](https://doi.org/10.1016/S0079-6611(98)00020-2)  
821 [6611\(98\)00020-2](https://doi.org/10.1016/S0079-6611(98)00020-2)
- 822 Matthäus, W., & Franck, H. (1992). Characteristics of major Baltic inflows—a statistical analysis.  
823 *Continental Shelf Research*, 12(12), 1375–1400. [https://doi.org/doi:10.1016/0278-](https://doi.org/10.1016/0278-4343(92)90060-W)  
824 [4343\(92\)90060-W](https://doi.org/10.1016/0278-4343(92)90060-W)
- 825 McDougall, T. J., & Barker, P. M. (2011). Getting started with TEOS-10 and the Gibbs Seawater  
826 (GSW) Oceanographic Toolbox. *SCOR/IAPSO WG127*, 28pp. [https://doi.org/ISBN 978-0-646-](https://doi.org/ISBN%20978-0-646-55621-5)  
827 [55621-5](https://doi.org/ISBN%20978-0-646-55621-5)
- 828 Meier, H. E. . (2007). Modeling the pathways and ages of inflowing salt- and freshwater in the Baltic  
829 Sea. *Estuarine, Coastal and Shelf Science*, 74(4), 610–627.  
830 <https://doi.org/10.1016/J.ECSS.2007.05.019>
- 831 Mohrholz, V. (2018). Major Baltic Inflow Statistics – Revised. *Frontiers in Marine Science*, 5, 384.  
832 <https://doi.org/10.3389/fmars.2018.00384>
- 833 Ollitrault, M., & Rannou, J.-P. (2013). *ANDRO: An Argo-based deep displacement dataset*.  
834 <https://doi.org/http://doi.org/10.17882/47077>



- 835 Placke, M., Meier, H. E. M., Gräwe, U., Neumann, T., Frauen, C., & Liu, Y. (2018). Long-Term  
836 Mean Circulation of the Baltic Sea as Represented by Various Ocean Circulation Models.  
837 *Frontiers in Marine Science*, 5(SEP), 287. <https://doi.org/10.3389/fmars.2018.00287>
- 838 Rasmus, K., Kiirikki, M., & Lindfors, A. (2015). Long-term field measurements of turbidity and  
839 current speed in the Gulf of Finland leading to an estimate of natural resuspension of bottom  
840 sediment. *Boreal Environment Research*, 20, 735–747.  
841 <http://www.borenv.net/BER/pdfs/ber20/ber20-735.pdf>
- 842 Reissmann, J. H., Burchard, H., Feistel, R., Hagen, E., Lass, H. U., Mohrholz, V., Nausch, G.,  
843 Umlauf, L., & Wiczorek, G. (2009). Vertical mixing in the Baltic Sea and consequences for  
844 eutrophication - A review. In *Progress in Oceanography* (Vol. 82, Issue 1, pp. 47–80).  
845 <https://doi.org/10.1016/j.pocean.2007.10.004>
- 846 Rubio, A., Gomis, D., Jordà, G., Espino, M., Rubio, A., Gomis, D., Jordà, G., & Espino, M. (2009).  
847 Estimating geostrophic and total velocities from CTD and ADCP data: Intercomparison of  
848 different methods. *JMS*, 77(1), 61–76. <https://doi.org/10.1016/J.JMARSYS.2008.11.009>
- 849 Scully, M. E. (2016). Mixing of dissolved oxygen in Chesapeake Bay driven by the interaction  
850 between wind-driven circulation and estuarine bathymetry. *Journal of Geophysical Research:*  
851 *Oceans*, 121(8), 5639–5654. <https://doi.org/10.1002/2016JC011924>
- 852 Siiriä, S., Roiha, P., Tuomi, L., Purokoski, T., Haavisto, N., & Alenius, P. (2019). Applying area-  
853 locked, shallow water Argo floats in Baltic Sea monitoring. *Journal of Operational*  
854 *Oceanography*, 12(1), 58–72. <https://doi.org/10.1080/1755876X.2018.1544783>
- 855 Sokolov, A., & Chubarenko, B. (2012). Wind Influence on the Formation of Nearshore Currents in  
856 the Southern Baltic: Numerical Modelling Results. *Archives of Hydroengineering and*  
857 *Environmental Mechanics*, 59(1–2), 37–48. <https://doi.org/10.2478/v10203-012-0003-3>
- 858 Soomere, T., & Keevallik, S. (2001). Anisotropy of moderate and strong winds in the Baltic Proper.  
859 In *Proc. Estonian Acad. Sci. Eng* (Vol. 7, Issue 1). [http://kirj.ee/public/va\\_te/t50-1-3.pdf](http://kirj.ee/public/va_te/t50-1-3.pdf)
- 860 Suhhova, I., Liblik, T., Lilover, M.-J., & Lips, U. (2018). A descriptive analysis of the linkage  
861 between the vertical stratification and current oscillations in the Gulf of Finland. *Boreal*  
862 *Environment Research*, 23, 83–103.
- 863 Suhhova, I., Pavelson, J., & Lagemaa, P. (2015). Variability of currents over the southern slope of  
864 the Gulf of Finland. *Oceanologia*, 57(2), 132–143. <https://doi.org/10.1016/j.oceano.2015.01.001>
- 865 Umlauf, L., Arneborg, L., Umlauf, L., & Arneborg, L. (2009). Dynamics of Rotating Shallow  
866 Gravity Currents Passing through a Channel. Part I: Observation of Transverse Structure.  
867 *Journal of Physical Oceanography*, 39(10), 2385–2401. <https://doi.org/10.1175/2009JPO4159.1>
- 868 Umlauf, L., & Burchard, H. (2005). Second-order turbulence closure models for geophysical  
869 boundary layers. A review of recent work. *Continental Shelf Research*, 25, 795–827.  
870 <https://doi.org/10.1016/j.csr.2004.08.004>
- 871 Väli, G., Meier, H. E. M., & Elken, J. (2013). Simulated halocline variability in the Baltic Sea and its  
872 impact on hypoxia during 1961-2007. *Journal of Geophysical Research: Oceans*, 118(12),



- 873 6982–7000. <https://doi.org/10.1002/2013JC009192>
- 874 Villaceros-Robineau, N., Herrera, J. L., Castro, C. G., Piedracoba, S., & Roson, G. (2013).  
875 Hydrodynamic characterization of the bottom boundary layer in a coastal upwelling system (Ría  
876 de Vigo, NW Spain). *Continental Shelf Research*, 68, 67–79.  
877 <https://doi.org/10.1016/j.csr.2013.08.017>
- 878 Wu, H., Deng, B., Yuan, R., Hu, J., Gu, J., Shen, F., Zhu, J., Zhang, J., Wu, H., Deng, B., Yuan, R.,  
879 Hu, J., Gu, J., Shen, F., Zhu, J., & Zhang, J. (2013). Detiding Measurement on Transport of the  
880 Changjiang-Derived Buoyant Coastal Current. *Journal of Physical Oceanography*, 43(11),  
881 2388–2399. <https://doi.org/10.1175/JPO-D-12-0158.1>
- 882 Wu, J. (1980). Wind-Stress coefficients over Sea surface near Neutral Conditions—A Revisit.  
883 *Journal of Physical Oceanography*, 10(5), 727–740. [https://doi.org/10.1175/1520-](https://doi.org/10.1175/1520-0485(1980)0102.0.co;2)  
884 [0485\(1980\)0102.0.co;2](https://doi.org/10.1175/1520-0485(1980)0102.0.co;2)
- 885 Zhurbas, V., Elken, J., Paka, V., Piechura, J., Väli, G., Chubarenko, I., Golenko, N., & Shchuka, S.  
886 (2012). Structure of unsteady overflow in the supsk furrow of the baltic sea. *Journal of*  
887 *Geophysical Research: Oceans*, 117(4), 4027. <https://doi.org/10.1029/2011JC007284>
- 888 Zhurbas, V., Väli, G., Golenko, M., & Paka, V. (2018). Variability of bottom friction velocity along  
889 the inflow water pathway in the Baltic Sea. *Journal of Marine Systems*, 184, 50–58.  
890 <https://doi.org/10.1016/J.JMARSYS.2018.04.008>
- 891 Zhurbas, V., Väli, G., & Kuzmina, N. (2021). Striped texture of submesoscale fields in the  
892 northeastern Baltic Proper: Results of very high-resolution modelling for summer season.  
893 *Oceanologia*. <https://doi.org/10.1016/J.OCEANO.2021.08.003>
- 894